

Origin of Aggregation-Induced Enhanced Emission: Role of Pseudo-Degenerate Electronic States of Excimers Formed in Aggregation Phases

Wataru Ota,^{†,‡} Ken Takahashi,[¶] Kenji Higashiguchi,[§] Kenji Matsuda,[§] and Tohru
Sato^{*,†,‡,||}

[†]*Fukui Institute for Fundamental Chemistry, Kyoto University, Sakyo-ku, Kyoto 606-8103,
Japan*

[‡]*Department of Molecular Engineering, Graduate School of Engineering, Kyoto University,
Nishikyo-ku, Kyoto 615-8510, Japan*

[¶]*Undergraduate School of Industrial Chemistry, Faculty of Engineering, Kyoto University,
Nishikyo-ku, Kyoto 615 8510, Japan*

[§]*Department of Synthetic Chemistry and Biological Chemistry, Kyoto University,
Nishikyo-ku, Kyoto 615-8510, Japan*

^{||}*Unit of Elements Strategy Initiative for Catalysts & Batteries, Kyoto University,
Nishikyo-ku, Kyoto 615-8510, Japan*

E-mail: tsato@scl.kyoto-u.ac.jp

Abstract

Origin of aggregation-induced enhanced emission (AIEE) is investigated considering cyano-substituted 1,2-bis(pyridylphenyl)ethene (CNPPE) as an example. On the basis of ONIOM calculations using the time-dependent density functional theory (TD-DFT), we found that pseudo-degeneracy of excimers formed in solid phase plays an important role in the appearance of AIEE. The electron density difference delocalized over molecules gives rise to small diagonal vibronic coupling constants (VCCs), which suggests that the internal conversion is more suppressed in solid phase than in solution phase. The reduction of the off-diagonal VCCs owing to the packing effect is elucidated by vibronic coupling density (VCD) analysis. The pseudo-degeneracy enables fluorescence from the high singlet excited states against Kasha’s rule because the electron density difference and the overlap density between the excited states vanish. A Hubbard model of a pseudo-degenerate electronic system is constructed to explain the vanishing mechanism. We propose the following design principle for AIEE: *a candidate molecule for AIEE should have pseudo-degenerate adiabatic electronic states in the aggregation phases originating from the excimer formation.*

Keywords

Introduction

In contrast to concentration quenching, aggregation-induced enhanced emission (AIEE) yields strong luminescence in the aggregation phases.^{1,2} The restriction of intramolecular motions is generally accepted as the reason behind AIEE, that is, the restriction of intramolecular rotations or vibrations arising from the physical constraint in the aggregation phases blocks non-radiative transition pathways.³ Hexaphenylsilole (HPS) is one of the AIEE dyes, and the restricted rotation of the side phenyl ring is found to be a key factor for AIEE.⁴⁻⁶ This is corroborated by quantum mechanical and molecular mechanical (QM/MM) calcula-

tions where the Huang–Rhys factors and reorganization energies at low-frequency modes are reduced in the solid phase compared to the gas phase owing to the packing effect.⁷ In addition, HPS having a bulky shape does not form a cofacial configuration in the solid phase,^{1,2} which is considered to prevent concentration quenching.

Cofacial aggregation is regarded as one of the reasons behind concentration quenching. This is because a destructive alignment of the transition dipole moment renders the lowest excited state that is symmetry forbidden.⁸ Nevertheless, some dyes have been reported to be emissive in spite of the formation of cofacial aggregations.^{9–16} In general, according to Kasha’s rule, emissions have been attributed to the lowest excited states.¹⁷ However, if all the radiative and non-radiative transitions from a higher excited state to all the lower excited states are suppressed, fluorescence from the higher excited state can be expected to occur against Kasha’s rule.

Sato *et al.* have already reported that, in fluorescent dopants employed in organic light-emitting diodes (OLEDs), radiative and non-radiative transitions from a triplet excited state T_n ($n > 1$) to all the lower triplet excited states can be suppressed due to the pseudo-degenerate electronic states.^{18–20} The pseudo-degeneracy leads to cancellation of the overlap density between the excited states, which generates T_n excitons with long lifetimes. This enables the fluorescence via higher triplets (FvHT) mechanism for OLEDs, that is fluorescence utilizing the reverse intersystem crossing (RISC) from T_n to singlets. FvHT is different from thermally activated delayed fluorescence (TADF) in that TADF undergoes the thermally activated RISC from T_1 to S_1 by decreasing the energy difference, $\Delta E_{S_1-T_1}$.^{21,22} The FvHT mechanism is proposed to explain the mechanism of electroluminescence in some OLED dopants with large $\Delta E_{S_1-T_1}$, where T_1 excitons cannot overcome the energy difference thermally.^{19,23}

A cyano-substituted 1,2-bis(pyridylphenyl)ethene (CNPPE) (Fig. 1) has been reported to exhibit the AIEE behavior in solid phase.²⁴ The rate constants of the non-radiative transitions are decreased from $> 1.0 \times 10^{10} \text{ s}^{-1}$ in CH_2Cl_2 solution to $5.0 \times 10^7 \text{ s}^{-1}$ in solid

phase. The rate constants of the radiative transitions are comparable between CH_2Cl_2 solution ($> 2.0 \times 10^7 \text{ s}^{-1}$) and solid phase ($1.3 \times 10^8 \text{ s}^{-1}$). Accordingly, the fluorescence quantum yield is increased from 0.002 to 0.72 by aggregation. Since CNPPE forms cofacial configurations in solid phase, the occurrence of concentration quenching is predicted. Some cofacial CNPPE molecules have C_i symmetry in the crystal structure. This suggests the possibility of pseudo-degenerate electronic states delocalized over the cofacial molecules. In this case, fluorescence from higher singlets than S_1 is expected to occur against Kasha's rule because the transitions between the excited states can be suppressed as in the case of the FvHT mechanism. The electronic states delocalized over molecules may decrease the vibronic coupling constants (VCCs).²⁵ These indicate that the internal conversion can be more suppressed in solid phase than in solution phase as long as excimer formation occurs in solid phase. This mechanism is different from what is proposed in styrylbenzene, i.e. di,[?] tri,^{??} and tetra(styryl)benzene,[?] which asserts that the origin of the AIEE behavior is attributed to blocking the trans-cis photoisomerization of stilbene unit in solid phase.

In this study, we investigated the role of pseudo-degeneracy in the appearance of AIEE considering CNPPE as an example. Vibronic coupling density (VCD) analyses were performed to elucidate the local picture of VCC.²⁶⁻²⁸ To explain the results obtained by the TD-DFT calculations, we discuss the electron density difference and overlap density in the pseudo-degenerate electronic system based on the Hubbard model.

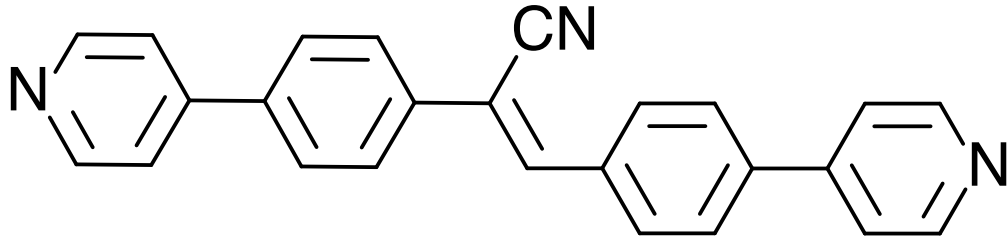


Figure 1: Chemical structure of cyano-substituted 1,2-bis(pyridyl)ethene (CNPPE).

Theory

We consider the internal conversion from an initial vibronic state $|\Phi_{mi}(\mathbf{r}, \mathbf{Q})\rangle$ associated with electronic m and vibrational mi states to a final vibronic state $|\Phi_{nj}(\mathbf{r}, \mathbf{Q})\rangle$. Here, $\mathbf{r} = (\mathbf{r}_1, \dots, \mathbf{r}_i, \dots, \mathbf{r}_N)$ is a set of N electronic coordinates, and $\mathbf{Q} = (Q_1, \dots, Q_\alpha, \dots, Q_M)$ is a set of M mass-weighted normal coordinates. Within the crude adiabatic approximation,^{29,30} the vibronic states are represented as the product of vibrational and electronic states fixed at the nuclear configuration \mathbf{R}_0 : $|\Phi_{mi}(\mathbf{r}, \mathbf{Q})\rangle = |\chi_{mi}(\mathbf{Q})\rangle |\Psi_m(\mathbf{r}; \mathbf{R}_0)\rangle$. \mathbf{R}_0 is chosen as the equilibrium nuclear configuration of the ground or excited optimized structures. The rate constant of the internal conversion from electronic state m to n is expressed as³¹

$$k_{n \leftarrow m}^{\text{IC}}(T) = \frac{2\pi}{\hbar} \sum_{\alpha} |V_{mn,\alpha}|^2 \sum_{ij} P_{mi}(T) |\langle \chi_{mi} | Q_{\alpha} | \chi_{nj} \rangle|^2 \delta(E_{mi} - E_{nj}), \quad (1)$$

where $P_{mi}(T)$ is the Boltzmann distribution function of the initial vibronic state at temperature T , and E_{mi} and E_{nj} are the eigenenergies of $|\Phi_{mi}(\mathbf{r}, \mathbf{Q})\rangle$ and $|\Phi_{nj}(\mathbf{r}, \mathbf{Q})\rangle$, respectively. E_{mi} is represented as the sum of electronic E_m and vibrational energies. $V_{mn,\alpha}$ is the off-diagonal VCC given by

$$V_{mn,\alpha} = \left\langle \Psi_m(\mathbf{r}; \mathbf{R}_0) \left| \left(\frac{\partial \hat{H}(\mathbf{r}, \mathbf{R})}{\partial Q_{\alpha}} \right)_{\mathbf{R}_0} \right| \Psi_n(\mathbf{r}; \mathbf{R}_0) \right\rangle, \quad (2)$$

where $\hat{H}(\mathbf{r}, \mathbf{R})$ is the molecular Hamiltonian, and \mathbf{R} is a set of nuclear configuration. $V_n := V_{nn}$ is called the diagonal VCC. Ignoring the Duschinsky effect, which means vibrational modes do not change during an excitation, the matrix element of the vibrational states is written as

$$\langle \chi_{mi} | Q_{\alpha} | \chi_{nj} \rangle = \langle n_{mi,\alpha} | Q_{\alpha} | n_{nj,\alpha} \rangle \prod_{\beta \neq \alpha} \langle n_{mi,\beta} | n_{nj,\beta} \rangle, \quad (3)$$

where $|n_{mi,\alpha}\rangle$ is a vibrational state of a single mode. The Franck–Condon (FC) overlap integral is expressed as³²

$$\begin{aligned} \langle n_{mi,\alpha} | n_{nj,\alpha} \rangle &= \sqrt{\frac{n_{mi,\alpha}! n_{nj,\alpha}!}{2^{n_{mi,\alpha} + n_{nj,\alpha}}}} e^{-\frac{1}{4}g_{n,\alpha}^2} \\ &\times \sum_{l=0}^{\min[n_{mi,\alpha}, n_{nj,\alpha}]} (-1)^{n_{mi,\alpha}-l} 2^l \frac{g_{n,\alpha}^{n_{mi,\alpha} + n_{nj,\alpha} - 2l}}{l!(n_{mi,\alpha} - l)!(n_{nj,\alpha} - l)!}. \end{aligned} \quad (4)$$

Here, $g_{n,\alpha}$ is the dimensionless diagonal VCC (the Huang–Rhys factor):

$$g_{n,\alpha} = \frac{V_{n,\alpha}}{\sqrt{\hbar\omega_{n,\alpha}^3}}, \quad (5)$$

where $\omega_{n,\alpha}$ is the angular frequency of vibrational mode α . In general, a rate constant of an internal conversion is small when diagonal and off-diagonal VCCs are small.³¹ Particularly, the dependence of the rate constant on the diagonal VCC is strong, and the reduction of the diagonal VCCs significantly contributes to the suppression of the internal conversion.³¹

Within a single mode approximation at 0 K, the rate constant of the internal conversion is reduced to³¹

$$k_{n \leftarrow m}^{\text{IC}}(T) = \frac{2\pi}{\hbar} |V_{mn,\alpha}|^2 \sum_j |\langle \chi_{mi} | Q_\alpha | \chi_{nj} \rangle|^2 \int_{E_{\min}}^{E_{\max}} \frac{1}{\sqrt{2\pi}\sigma} e^{-\frac{(E - (E_{mi} - E_{nj}))^2}{2\sigma^2}} dE, \quad (6)$$

where the delta function is replaced with the Gaussian function which represents the density of states with the linewidth σ .

In addition to the internal conversion, vibrational relaxation from FC to adiabatic (AD) states is a non-radiative process that should suppress for emission.³¹ Within the crude adiabatic representation assuming the harmonic approximation, the reorganization energy due to vibrational relaxation is evaluated by

$$\Delta E = \sum_{\alpha} \frac{V_{n,\alpha}^2}{2\omega_{n,\alpha}^2}. \quad (7)$$

Thus, the reduction of the diagonal VCCs leads to the small reorganization energy that depends on the square of the diagonal VCCs.

The VCD is expressed as the density form of the VCC:^{26–28}

$$V_{mn,\alpha} = \int d\mathbf{x} \eta_{mn,\alpha}(\mathbf{x}), \quad (8)$$

where $\mathbf{x} = (x, y, z)$ is a three dimensional coordinate. The diagonal VCD $\eta_{n,\alpha}(\mathbf{x}) := \eta_{nn,\alpha}(\mathbf{x})$ is defined by

$$\eta_{n,\alpha}(\mathbf{x}) = \Delta\rho_{nn}(\mathbf{x}) \times v_\alpha(\mathbf{x}). \quad (9)$$

Here, $\Delta\rho_{nm}(\mathbf{x})$ is the electron density difference between $|\Psi_n(\mathbf{r}; \mathbf{R}_0)\rangle$ and the reference state $|\Psi_m(\mathbf{r}; \mathbf{R}_0)\rangle$:

$$\Delta\rho_{nm}(\mathbf{x}) = \langle \Psi_n(\mathbf{r}; \mathbf{R}_0) | \hat{\rho}(\mathbf{x}) | \Psi_n(\mathbf{r}; \mathbf{R}_0) \rangle - \langle \Psi_m(\mathbf{r}; \mathbf{R}_0) | \hat{\rho}(\mathbf{x}) | \Psi_m(\mathbf{r}; \mathbf{R}_0) \rangle. \quad (10)$$

$|\Psi_m(\mathbf{r}; \mathbf{R}_0)\rangle$ is taken as the electronic state in the equilibrium nuclear configuration. $\hat{\rho}(\mathbf{x})$ is the electron density operator defined by

$$\hat{\rho}(\mathbf{x}) = \sum_{ij} \sum_{\sigma\tau} \hat{c}_{i\sigma}^\dagger \hat{c}_{j\tau} \psi_{i\sigma}^*(\mathbf{x}) \psi_{j\tau}(\mathbf{x}), \quad (11)$$

where $\psi_{i\sigma}^*(\mathbf{x})$ and $\psi_{j\tau}(\mathbf{x})$ are spatial orbitals, and $\hat{c}_{i\sigma}^\dagger$ and $\hat{c}_{j\tau}$ are creation and annihilation operators, respectively. i and j refer to the orbital indices, and σ and τ refer to the spin indices. $v_\alpha(\mathbf{x})$ is the potential derivative expressed as

$$v_\alpha(\mathbf{x}) = \left(\frac{\partial u(\mathbf{x})}{\partial Q_\alpha} \right)_{\mathbf{R}_0}, \quad (12)$$

where $u(\mathbf{x})$ is the electron-nucleus potential acting on a single electron.

The off-diagonal VCD is defined by

$$\eta_{mn,\alpha}(\mathbf{x}) = \rho_{mn}(\mathbf{x}) \times v_{\alpha}(\mathbf{x}), \quad (13)$$

where $\rho_{mn}(\mathbf{x})$ is the overlap density between $|\Psi_m(\mathbf{r}; \mathbf{R}_0)\rangle$ and $|\Psi_n(\mathbf{r}; \mathbf{R}_0)\rangle$:

$$\rho_{mn}(\mathbf{x}) = \langle \Psi_m(\mathbf{r}; \mathbf{R}_0) | \hat{\rho}(\mathbf{x}) | \Psi_n(\mathbf{r}; \mathbf{R}_0) \rangle. \quad (14)$$

The VCD enables us to understand the vibronic couplings (VCs) arising from the electronic factor $\Delta\rho_{nm}(\mathbf{x})$ or $\rho_{mn}(\mathbf{x})$ and the vibrational factor $v_{\alpha}(\mathbf{x})$. It should be noted that the disappearance of $\Delta\rho_{nm}(\mathbf{x})$ and $\rho_{mn}(\mathbf{x})$ gives rise to the suppression of the internal conversions via the reduction of $V_{n,\alpha}$ and $V_{mn,\alpha}$, respectively. Since the transition dipole moment also depends on $\rho_{mn}(\mathbf{x})$,³¹ the disappearance of $\rho_{mn}(\mathbf{x})$ suppresses both the radiative and non-radiative transitions.

Methods of calculations

Figure 2 (a) shows the crystal structure of the CNPPE solid.²⁴ We modeled the CNPPE solid as a dimer with a cofacial configuration (Fig. 2 (b)), Dimer Model **1**, where the cofacial dimer was calculated by the QM method and the surrounding 16 molecules were calculated by the MM method based on the ONIOM (our own n -layered integrated molecular orbital and molecular mechanics) approach.^{33,34} Dimer Model **1** has C_i symmetry. The other dimer models aligned in different directions, Dimer Model **2** and Dimer Model **3** (see Fig. S1 in the Supplementary Information), having C_1 symmetry were also investigated. The ground and excited states of the QM region were computed at the M06-2X/6-31G(d,p) and TD-M06-2X/6-31G(d,p) levels of theory, respectively, whereas the MM region was computed using the universal force field (UFF). The M06-2X functional was employed to incorporate dispersion interactions between adjacent molecules.[?] The coordinates of the MM region

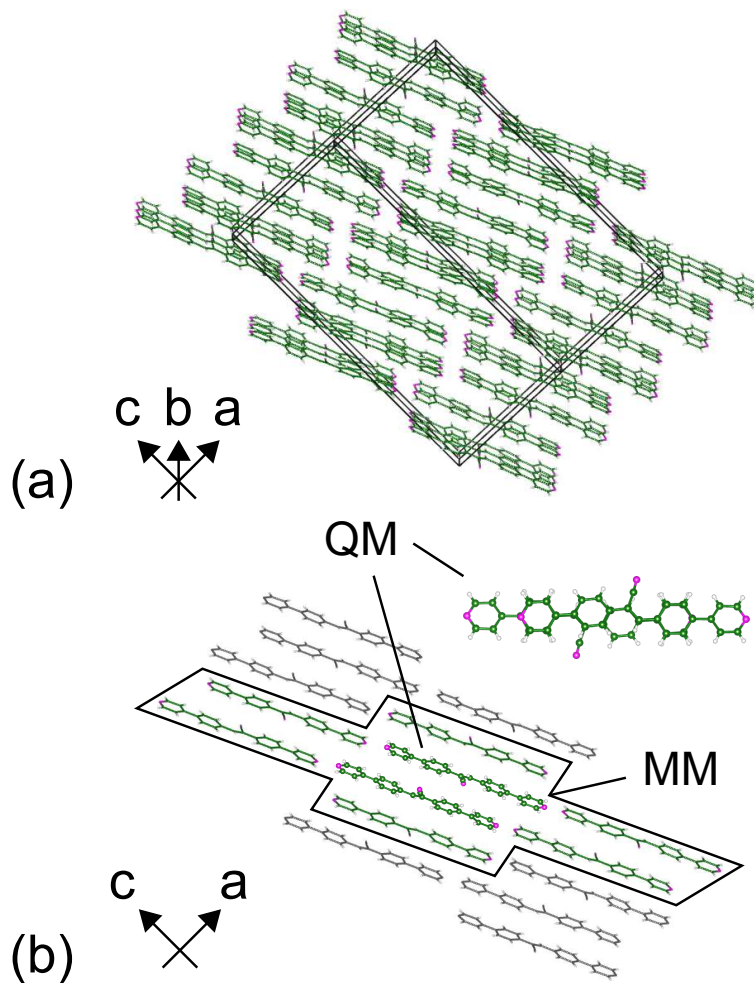


Figure 2: (a) Crystal structure of CNPPE solid.²⁴ (b) Dimer Model **1** for the CNPPE solid where centered cofacial molecules with C_i symmetry are selected as the QM region and the surrounding 16 molecules are selected as the MM region.

were fixed during the geometry optimizations and vibrational analyses for the ground and excited states.

The CNPPE in CH_2Cl_2 solution was modeled as a single molecule with C_1 symmetry. The ground and excited states of a single molecule in solution, Monomer Model, were computed at the M06-2X/6-31G(d,p) and TD-M06-2X/6-31G(d,p) levels of theory, respectively, including the solvent effect through the polarizable continuum model (PCM).³⁵ The above calculations were carried out using the Gaussian 09.^{36,37} The VCCs and VCD were calculated using our own code.

Results and discussion

Vibronic coupling constants (VCCs) and vibronic coupling density (VCD)

There are a few possibilities for selecting dimers from the crystal structure. The total energies of excited states of the three types of dimer models were compared (Fig. S2). The S_1 and S_2 states of Dimer Model 1 are energetically more stable than those of the other dimer models, and the fluorescence from Dimer Model 1 is expected. Therefore, we concentrate ourselves on Dimer Model 1. Table 1 lists the excited states of Dimer Model 1 at the S_0 and S_2 optimized structures. From the selection rule of the electric dipole transition, S_1 (A_g) is symmetry-forbidden and S_2 (A_u) is symmetry-allowed (Laporte rule). Although, according to Kasha's rule, an emission does not occur from the second excited states, the fluorescence from S_2 is possible if all the transitions from S_2 to S_1 are suppressed.

Table 1: Excited states of Dimer Model 1 at the S_0 and S_2 optimized structures. f denotes the oscillator strength.

	State	Excitation Energy		f	Major Configuration (CI coefficient)
		eV	nm		
@ S_0	$S_1(A_g)$	3.7359	331.88	0.0000	HO-1 \rightarrow LU+1 (0.306) HO \rightarrow LU (0.622)
	$S_2(A_u)$	3.9052	317.49	2.2807	HO-1 \rightarrow LU (0.366) HO \rightarrow LU+1 (0.585)
@ S_2	$S_1(A_g)$	3.1397	394.89	0.0000	HO-1 \rightarrow LU+1 (0.212) HO \rightarrow LU (0.664)
	$S_2(A_u)$	3.3074	374.86	1.8099	HO-1 \rightarrow LU (0.215) HO \rightarrow LU+1 (0.663)

Figures 3 (a) and (b) show the diagonal VCCs of $S_0@S_2$ and $S_1@S_2$, respectively. Furthermore, Figs. 3 (c) and (d) show the off-diagonal VCCs of $S_0@S_2 \leftarrow S_2@S_2$ and $S_1@S_2 \leftarrow S_2@S_2$, respectively. The diagonal VCCs of $S_1@S_2$ are extremely small where the largest VCC of vibrational mode 233 is 0.79×10^{-4} a.u. In addition, both the off-diagonal VCCs of $S_1@S_2 \leftarrow S_2@S_2$ and $S_0@S_2 \leftarrow S_2@S_2$ are small. These results indicate that the inter-nal conversions from S_2 to S_0 as well as to S_1 are suppressed while the radiative transition

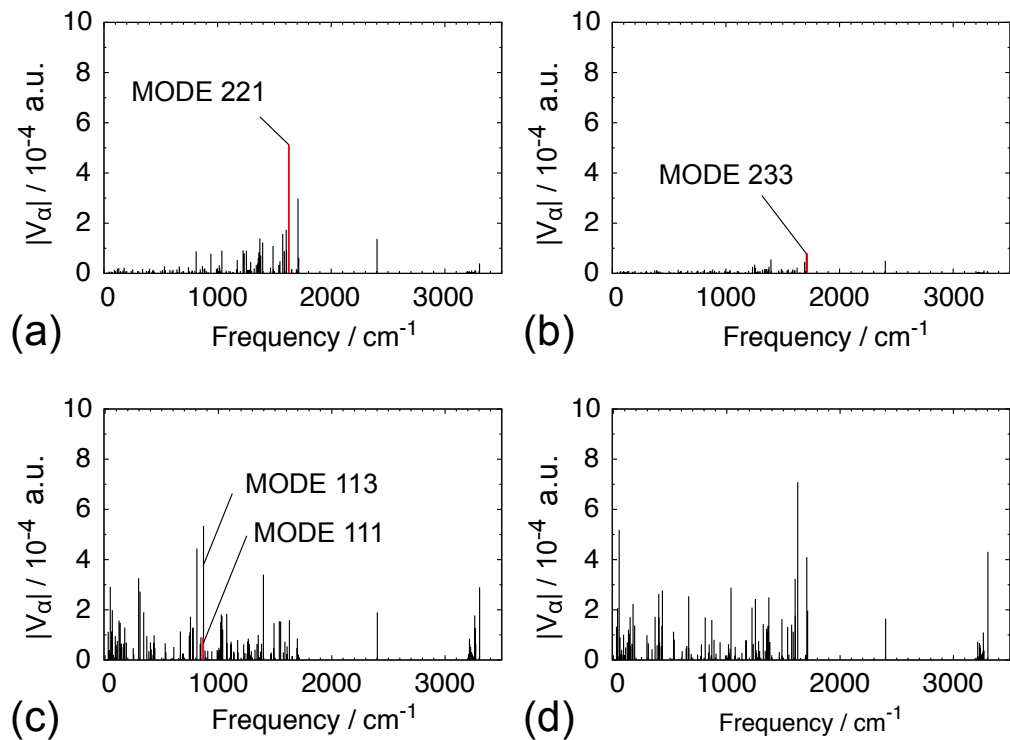


Figure 3: Diagonal VCCs of (a) $S_0@S_2$ and (b) $S_1@S_2$ as well as off-diagonal VCCs of (c) $S_0@S_2 \leftarrow S_2@S_2$ and (d) $S_1@S_2 \leftarrow S_2@S_2$ for Dimer Model 1.

between S_2 and S_0 is enabled with the large oscillator strength (see Table 1). It should be noted, because of the extremely small diagonal VCCs of $S_1@S_2$, that the internal conversion from S_2 to S_1 is suppressed, thereby enabling the fluorescence from S_2 .

Figures 4 (a) and (b) present the frontier orbitals and orbital levels at the S_2 optimized structure, respectively. The adiabatic wave functions are delocalized over the molecules, thereby indicating the excimer formation in solid phase. Herein, an excimer is defined as an excited state delocalized over a dimer. The AD S_2 is an excimer state without an intermolecular charge transfer character. The relaxed S_1 also forms an excimer state similar to S_2 . In the present case, the delocalized electronic states are obtained because Dimer Model 1 belongs to C_i symmetry even in the AD state. The NHOMO and HOMO as well as the LUMO and NLUMO of the excimer are pseudo-degenerate, which are approximately

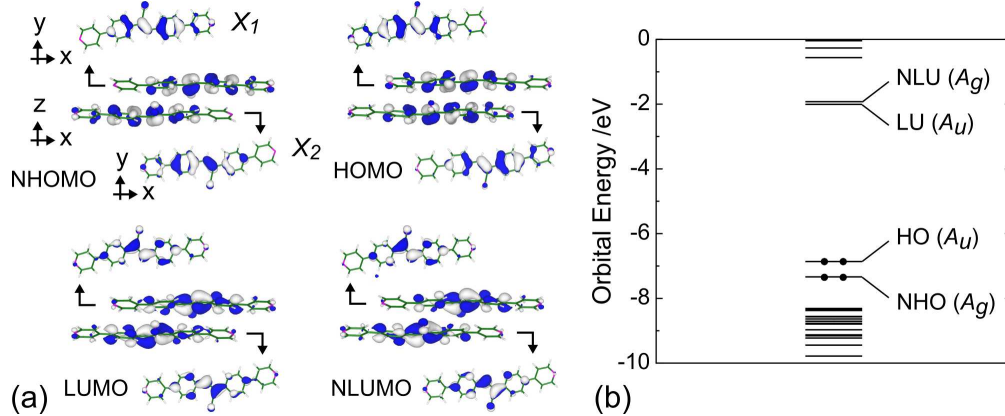


Figure 4: (a) Frontier orbitals and (b) orbital levels of Dimer Model **1** at the S_2 optimized structure. X_1 and X_2 are the constituent molecules of Dimer Model **1**. Isosurface values of the frontier orbitals are 3.0×10^{-2} a.u.

expressed as

$$\psi_{\text{NHO}} \approx \frac{1}{\sqrt{2}}(\phi_{\text{HO}}(X_1) + \phi_{\text{HO}}(X_2)), \quad (15)$$

$$\psi_{\text{HO}} \approx \frac{1}{\sqrt{2}}(\phi_{\text{HO}}(X_1) - \phi_{\text{HO}}(X_2)), \quad (16)$$

$$\psi_{\text{LU}} \approx \frac{1}{\sqrt{2}}(\phi_{\text{LU}}(X_1) - \phi_{\text{LU}}(X_2)), \quad (17)$$

$$\psi_{\text{NLU}} \approx \frac{1}{\sqrt{2}}(\phi_{\text{LU}}(X_1) + \phi_{\text{LU}}(X_2)), \quad (18)$$

where $\phi_{\text{HO/LU}}(X_1/X_2)$ denotes the HOMO/LUMO of molecule X_1/X_2 comprising the model. $\phi_{\text{HO/LU}}(X_2)$ are obtained by a symmetry operation of $\phi_{\text{HO/LU}}(X_1)$. The frontier orbitals of the excimer are represented as the linear combinations of the HOMOs and LUMOs of the constituents with opposite signs.

S_1 mainly consists of the HOMO-LUMO and NHOMO-NLUMO excited configurations, whereas S_2 mainly consists of the HOMO-NLUMO and NHOMO-LUMO excited configurations (Table 1). Since the NHOMO/HOMO and LUMO/NLUMO are pseudo-degenerate, S_1 and S_2 are pseudo-degenerate. Figure 5 (a) and (b) show the electron density differences of $S_2@S_2-S_0@S_2$, $\Delta\rho_{20}$, and $S_1@S_2-S_0@S_2$, $\Delta\rho_{10}$, respectively. $\Delta\rho_{20}$ and $\Delta\rho_{10}$ exhibit similar distributions. On the contrary, the electron density difference of $S_2@S_2-S_1@S_2$, $\Delta\rho_{21}$

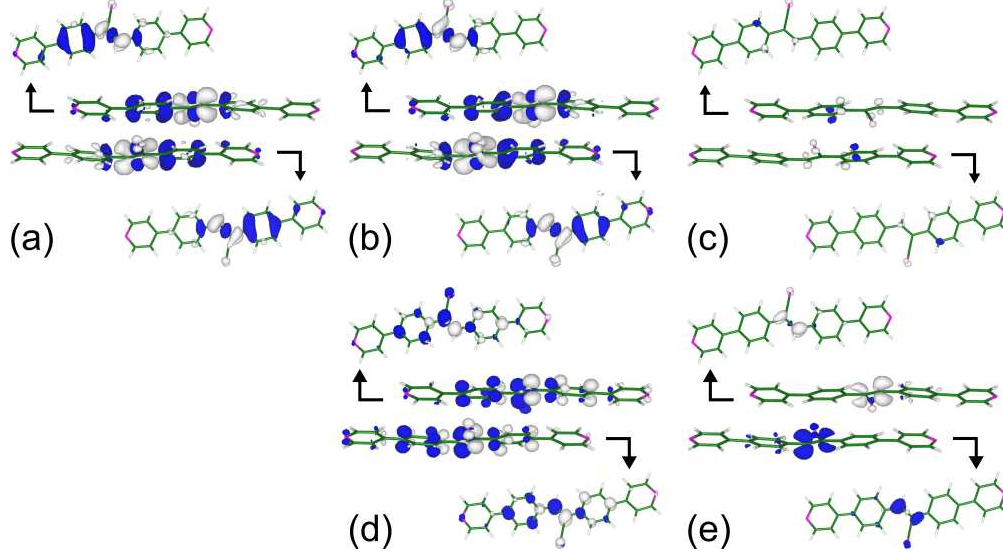


Figure 5: Electron density differences of (a) $S_1@S_2-S_0@S_2$, (b) $S_2@S_2-S_0@S_2$, and (c) $S_2@S_2-S_1@S_2$ of Dimer model 1. Isosurface values are 1.0×10^{-3} a.u. Overlap densities of (d) $S_2@S_2-S_0@S_2$, and (e) $S_2@S_2-S_1@S_2$ of Dimer model 1. Isosurface values are 2.0×10^{-3} a.u.

(Fig. 5 (c)) exhibits an extremely small distribution. This leads to the small diagonal VCD of $S_1@S_2$, resulting in the small diagonal VCCs of $S_1@S_2$. Figures 5 (d) and (e) show the overlap densities of $S_2@S_2-S_0@S_2$, ρ_{20} , and $S_2@S_2-S_1@S_2$, ρ_{21} , respectively. ρ_{21} exhibits a smaller distribution than that of ρ_{20} . The small ρ_{21} contributes to the small off-diagonal VCCs of $S_1@S_2 \leftarrow S_2@S_2$. From the distributions of the overlap densities, the off-diagonal VCCs of $S_0@S_2 \leftarrow S_2@S_2$ could be much larger than those of $S_1@S_2 \leftarrow S_2@S_2$. However, the values of these off-diagonal VCCs are comparable (Figs. 3 (c) and (d)) because ρ_{20} is symmetrically localized on the atoms while ρ_{21} is localized on the bonds. In general, an overlap density that is symmetrically localized on atoms weakly couples to a potential derivative, resulting in small off-diagonal VCCs.³¹ Therefore, the off-diagonal VCCs of $S_0@S_2 \leftarrow S_2@S_2$ are not large.

Consequently, the small electron density difference and overlap density between the pseudo-degenerate S_1 and S_2 excited states leads to the extremely small diagonal VCCs of $S_1@S_2$ and the small off-diagonal VCCs of $S_1@S_2 \leftarrow S_2@S_2$. We discuss the mechanism of the vanished electron density difference and overlap density in the pseudo-degenerate

electronic system using the Hubbard model in Sec. .

Below, we compare the VCs of Dimer Model **1** in solid phase with that of Monomer Model in solution phase. The reducible representation of vibrational modes for the monomer belonging to C_1 symmetry contains only A irreducible representations, and the number of the vibrational modes is

$$\Gamma_{\text{vib}}(C_1) = 129A, \quad (19)$$

where all vibrational modes are vibronic active modes that provide the non-zero diagonal and off-diagonal VCCs. On the other hand, the reducible representation for the dimer belonging to C_i symmetry is decomposed as

$$\Gamma_{\text{vib}}(C_i) = 132A_g + 132A_u, \quad (20)$$

where A_g and A_u are the totally and non-totally symmetric modes, respectively. The vibronic active mode for the diagonal VC is A_g and that for the off-diagonal VC is A_u . Therefore, the number of the vibronic active modes is almost the same in the monomer and dimer although the total number of vibrational modes is higher in the dimer. The numbers of irreducible representations of vibrational modes in excimers with C_i , C_2 , and C_s symmetry are summarized in Section S2.

Figures 6 (a) and (b) show the diagonal VCCs of Monomer Model in the FC S_1 state and Dimer Model **1** in the FC S_2 state, respectively. The diagonal VCCs are greatly reduced due to the excimer formation where the largest VCC of mode 109 in Monomer Model is 8.42×10^{-4} a.u. and that of mode 230 in Dimer Model **1** is 5.27×10^{-4} a.u. This result indicates that the internal conversion from S_2 to S_0 in Dimer Model **1** is suppressed in comparison with the one from S_1 to S_0 in Monomer Model because the rate constant of the internal conversion is strongly correlated with the diagonal VCCs.³¹ The off-diagonal VCCs of $S_0@S_1 \leftarrow S_1@S_1$ for Monomer Model are presented in Fig. 6 (c). The off-diagonal VCCs of Dimer Model **1** (Fig. 3 (c)) are smaller than those of Monomer Model. For example,

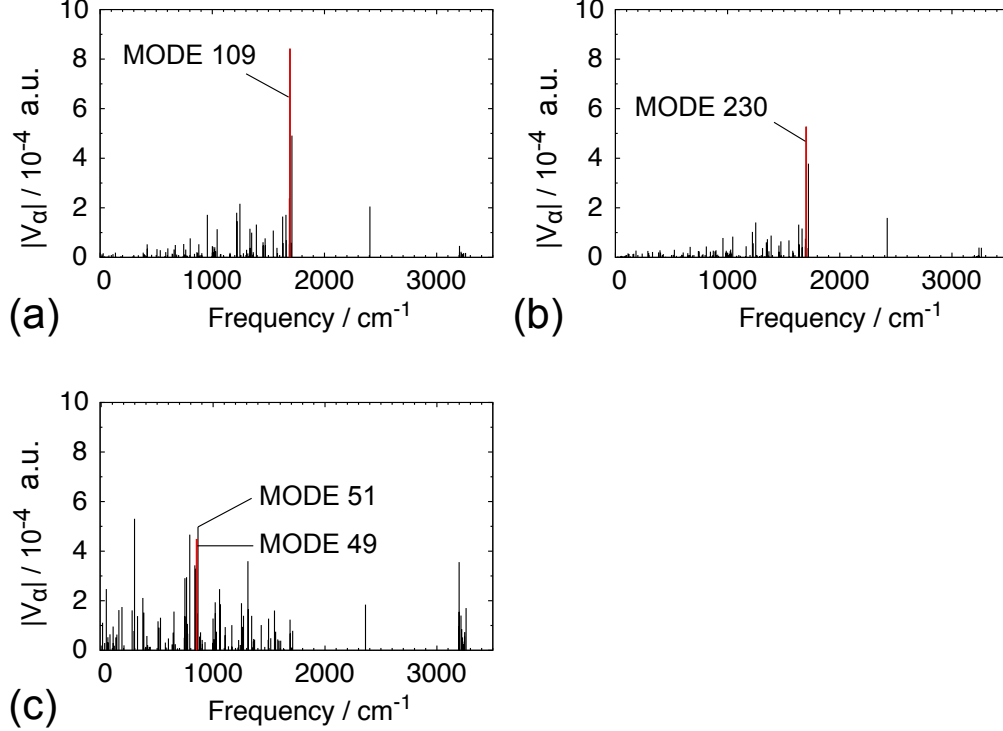


Figure 6: Diagonal VCCs (a) of Monomer Model in the FC S_1 state and (b) of Dimer Model **1** in the FC S_2 state. (c) Off-diagonal VCCs of $S_0@S_1 \leftarrow S_1@S_1$ of Monomer Model.

the off-diagonal VCC of mode 49 in Monomer Model is 4.49×10^{-4} and that of mode 111 in Dimer Model **1**, corresponding to mode 49 in Monomer Model, is 0.89×10^{-4} a.u. The reduction of the off-diagonal VCCs in Dimer Model **1** also contributes to the suppression of the internal conversion.

The off-diagonal VCCs of the maximum coupling modes are comparable between Monomer Model (5.30×10^{-4} a.u.) and Dimer Model **1** (5.33×10^{-4} a.u.). In contrast, the diagonal VCC of the maximum coupling mode at 1692 cm^{-1} for Monomer Model (8.42×10^{-4} a.u.) is larger than that at 1701 cm^{-1} for Dimer Model **1** (5.27×10^{-4} a.u.). The differences of electronic energies between S_1 and S_0 is 3.14 eV for Monomer Model, and between S_2 and S_0 is 3.51 eV for Dimer Model **1**. Suppose that $V_{mn,\alpha} = 5.00 \times 10^{-4}$ a.u., $\omega_\alpha = 1700 \text{ cm}^{-1}$, $E_m - E_n = 3.0 \text{ eV}$, $\sigma = 500 \text{ cm}^{-1}$, $E_{\min} = -11500 \text{ cm}^{-1}$, and $E_{\max} = 11500 \text{ cm}^{-1}$ in Eq. (6), the rate constants of the internal conversion considering only a diagonal VCC maximum coupling mode are estimated to be $1.569 \times 10^{10} \text{ s}^{-1}$ for Monomer Model and $5.651 \times 10^7 \text{ s}^{-1}$

for Dimer Model **1**. The ratio of the rate constants of Monomer Model to Dimer Model **1** is in the order of 10^2 . These are in good agreement with experiments ($> 1.0 \times 10^{10} \text{ s}^{-1}$ in CH_2Cl_2 solution and $5.0 \times 10^7 \text{ s}^{-1}$ in solid phase).²⁴ Therefore, the reduction of the diagonal VCCs mainly contributes to the suppression of the internal conversion in the solid phase. It should be noted however that the rate constant depends on the broadening of the density of states σ (Table S4).[?] The broadening of the density of states occurs by the interactions with the surrounding environment and vibronic couplings. Since the evaluation of these effects is out of scope in the present study, σ was treated as an external parameter. We previously adopted the values of σ ranging from 300 to 1200 cm^{-1} to compute the absorption spectra that reproduces the experimental results.^{??} We employed $\sigma = 500 \text{ cm}^{-1}$ in estimating the rate constants, and obtained the good agreement of the experimental values. Even when different σ is used, the ratios of the rate constants of Monomer Model to Dimer Model **1** do not drastically change (Table S4).

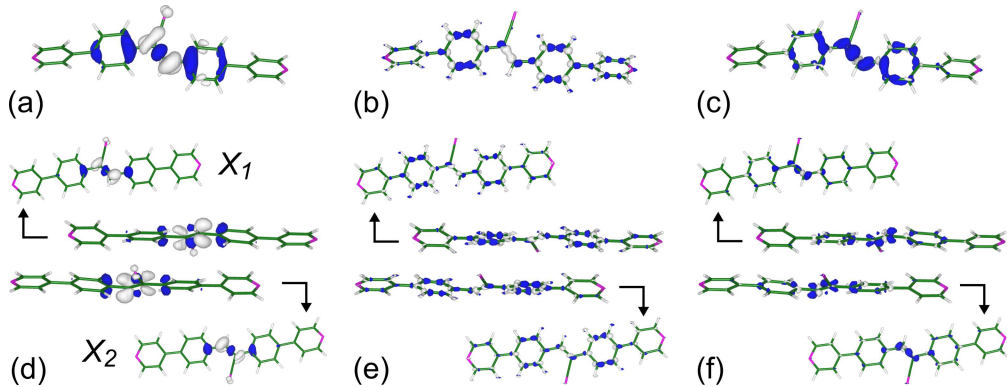


Figure 7: (a) Electron density difference, $\Delta\rho_{nm}(\mathbf{x})$, (b) potential derivative, $v_{\alpha}(\mathbf{x})$, and (c) diagonal VCD, $\eta_{n,\alpha}(\mathbf{x})$, of Monomer Model in the FC S_1 state for the maximum coupling mode (mode 109). (d) $\Delta\rho_{nm}(\mathbf{x})$, (e) $v_{\alpha}(\mathbf{x})$, and (f) $\eta_{n,\alpha}(\mathbf{x})$ of Dimer Model **1** in the FC S_2 state for the maximum coupling mode (mode 230). Isosurface values of $\Delta\rho_{nm}(\mathbf{x})$, $v_{\alpha}(\mathbf{x})$, and $\eta_{n,\alpha}(\mathbf{x})$ are 2.0×10^{-3} , 1.0×10^{-2} , and 1.0×10^{-5} a.u., respectively.

To determine the origin of the VCCs, VCD analyses are performed. Figure 7 shows the results of the diagonal VCD analyses for the maximum coupling mode of Monomer Model and Dimer Model **1**. $\Delta\rho_{nm}(\mathbf{x})$ of Monomer Model strongly couples with $v_{\alpha}(\mathbf{x})$ of mode 109, leading to a large $\eta_{n,\alpha}(\mathbf{x})$ that is particularly localized on the C=C bond. Thus, the spatial

integration of $\eta_{n,\alpha}(\mathbf{x})$ of mode 109 provides the largest VCC. $\Delta\rho_{nm}(\mathbf{x})$, $v_\alpha(\mathbf{x})$, and $\eta_{n,\alpha}(\mathbf{x})$ of Dimer Model **1** are delocalized over the molecules. In general, delocalized $\Delta\rho_{nm}(\mathbf{x})$ and $v_\alpha(\mathbf{x})$ yield smaller diagonal VCCs than localized ones.²⁵ $\Delta\rho_{nm}(\mathbf{x})$ of X_1 (or X_2) exhibits a similar distribution to that of Monomer Model. The value of $\Delta\rho_{nm}(\mathbf{x})$ of X_1 is one half of that of Monomer Model because the spatial integration of $\Delta\rho_{nm}(\mathbf{x})$ is zero by definition. In addition, $v_\alpha(\mathbf{x})$ of X_1 is $1/\sqrt{2}$ times that of Monomer Model owing to the normalized condition of vibrational modes. Since $\eta_{n,\alpha}(\mathbf{x})$ is expressed as the product of $\Delta\rho_{nm}(\mathbf{x})$ and $v_\alpha(\mathbf{x})$, the diagonal VCD of X_1 is $1/(2\sqrt{2})$ times that of Monomer Model. Therefore, the diagonal VCCs of Dimer Model **1**, obtained by the spatial integration of the diagonal VCD, are $1/\sqrt{2}$ times those of the Monomer Model. The ratio of the largest diagonal VCC of Dimer Model **1** to Monomer Model is 0.626, which is approximately equal to $1/\sqrt{2} \approx 0.707$; however deviation occurs because the structures of X_1 and the monomer are not the same.

In Dimer Model **1**, the reduction of the diagonal VCCs results from the delocalized electronic states. In contrast, in Dimer Model **2** the electronic states are localized on a single molecule in the adiabatic excited states (Fig. S3), which causes the properties of excited states to be similar to those of the monomer. Therefore, the reduction of the diagonal VCCs is not expected in Dimer Model **2**. The electronic states are delocalized over molecules in Dimer Model **3** (Fig. S4), suggesting small diagonal VCCs as in the case for Dimer Model **1**.

The driving force of the excimer formation is the diagonal VCCs. Figure 8 (a) shows the effective mode for the excimer formation of Dimer Model **1** in the FC S_2 state. The effective mode is defined by the sum of normal modes weighted by the diagonal VCCs:

$$\xi = \sum_{\alpha} \frac{V_{n,\alpha}}{\sqrt{\sum_{\alpha} |V_{n,\alpha}|^2}} Q_{\alpha}, \quad (21)$$

which is the steepest descent direction of the vibrational relaxation.³⁸ The effective mode is the intramolecular vibration rather than the intermolecular one. This indicates that the

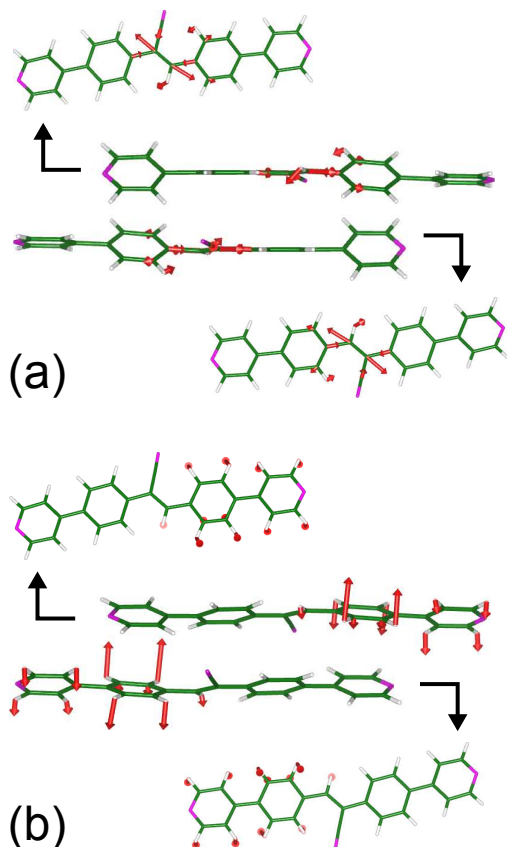


Figure 8: (a) Effective mode for the excimer formation of Dimer Model **1** in the FC S_2 state. This is an intramolecular vibration. (b) Vibrational mode 111 of Dimer Model **1** in the AD S_2 state; the off-diagonal VCC of this mode is decreased due to the packing effect. This is an intermolecular vibration.

excimer formation is induced by the intramolecular vibration.

Figure 9 shows the results of the off-diagonal VCD analyses of mode 49 for Monomer Model and mode 111 for Dimer Model **1**. $v_{49}(\mathbf{x})$ of Monomer Model is distributed over the stilbene unit. On the contrary, $v_{111}(\mathbf{x})$ of Dimer Model **1** is localized on one side of the stilbene unit. This is because vibrational mode 111 is the intermolecular vibration (Fig. 8 (b)), i.e. torsional mode of stilbene unit, that is restricted by the surrounding molecules in the solid phase. In other words, the localization of $v_{\alpha}(\mathbf{x})$ arises from the packing effect. As a result, $\eta_{mn,\alpha}(\mathbf{x})$ of Dimer Model **1** is also localized on one side of the stilbene unit giving the small off-diagonal VCCs. The degree of localization of $v_{\alpha}(\mathbf{x})$ is expected to depend on the types of vibrational modes. The off-diagonal VCC of mode 51 in Monomer Model is

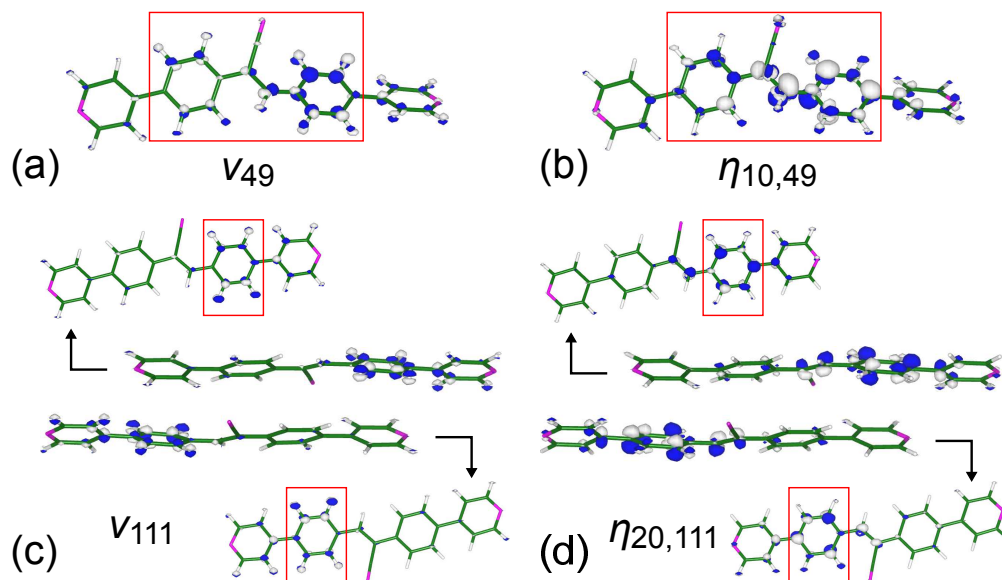


Figure 9: (a) Potential derivative, $v_\alpha(\mathbf{x})$, and (b) off-diagonal VCD, $\eta_{mn,\alpha}(\mathbf{x})$, of $S_1@S_1$ - $S_0@S_1$ of Monomer Model. (c) $v_\alpha(\mathbf{x})$ and (b) $\eta_{mn,\alpha}(\mathbf{x})$ of $S_2@S_2$ - $S_0@S_2$ of Dimer Model **1**. Isosurface values of $v_\alpha(\mathbf{x})$ and $\eta_{mn,\alpha}(\mathbf{x})$ are 1.0×10^{-2} and 1.0×10^{-5} a.u., respectively.

4.98×10^{-4} a.u. (Fig. 6 (c)), which is comparable to that of mode 113 in Dimer Model **1**, 5.34×10^{-4} a.u., (Fig. 3 (c)). Figure S5 shows $v_{51}(\mathbf{x})$ of Monomer Model and $v_{113}(\mathbf{x})$ of Dimer Model **1**. $v_{113}(\mathbf{x})$ of Dimer Model **1** is distributed over the stilbene unit rather than localized on one side of the stilbene unit in a similar manner to $v_{51}(\mathbf{x})$ of Monomer Model. This is because vibrational mode 113 is the intramolecular vibration that is not easily affected by the surrounding molecules (Fig. S5). Therefore, the off-diagonal VCCs corresponding to these modes are not reduced by the packing effect. The packing effect in solid phase is visualized by the potential derivative.

The small diagonal VCCs contribute to the suppression not only of the internal conversion but also of the vibrational relaxation.³¹ The reorganization energies due to vibrational relaxation were calculated to be $\Delta E = 0.582$ eV for Monomer Model and $\Delta E = 0.275$ eV for Dimer Model **1**. For Monomer Model, since the potential energy surfaces of low-frequency torsional modes were not approximated to harmonic potentials, the reorganization energies for these vibrational modes were evaluated from the potential energy surfaces³¹ instead of using Eq. (7) (Fig. S6). The reorganization energy of Dimer Model **1** is smaller than that

of Monomer Model, and suppressed vibrational relaxation is expected in Dimer Model **1**.

Furthermore, we calculated the electronic states of Decamer Model for the CNPPE solid (Fig. S7). Decamer Model has a large oscillator strength in the FC S_8 state (Table S7), and the S_8 exciton is expected to be generated by absorption. The electron density difference between the FC S_8 and S_0 states is delocalized as in the case for the combination of Dimer Model **1** and **2** (Fig. S8). The electronic states of Dimer Model **2** are localized on a single molecule after vibrational relaxation. Therefore, Decamer Model can be reduced to Dimer Model **1** in the adiabatic excited states. Thus, the modeling of the CNPPE solid using Dimer Model **1** is considered to be reasonable.

We also performed the calculations of Dimer Model **1** using the long-range corrected ω B97X-D functional⁷ in order to check the robustness of the results. S_2 (A_u) consisting of the HOMO-1-LUMO and HOMO-LUMO+1 excited configurations is symmetry-allowed from the Laporté rule (Table S8). In addition, the frontier orbitals in the AD S_2 state are delocalized over the molecules (Fig. S9), and the excited states do not have a charge transfer character. Therefore, the same conclusions as using the M06-2X functional can be deduced.

Hubbard model in a pseudo-degenerate electronic system

In this section, we discuss the disappearance mechanism of the electron density difference and overlap density based on the Hubbard model. We consider an excited electronic structure of a system consisting of the same molecules X_1 and X_2 (Fig. 10 (a)). Each molecule is not necessarily symmetric, but the dimer is assumed to have a symmetry such as C_i , C_2 , or C_s . For simplicity, only the HOMOs and LUMOs of X_1 and X_2 are considered. The energy gap between the HOMO and LUMO is expressed as ϵ . The hopping integrals for the HOMO-HOMO, LUMO-LUMO, and HOMO-LUMO between X_1 and X_2 are denoted by t_1 , t_2 , and t_3 , respectively. The Coulomb interactions for the HOMO-HOMO and HOMO-LUMO within X_1 or X_2 are denoted by U_1 and U_2 , respectively. Considering only a single excitation as done by the TD-DFT calculations, there are 9 electronic configurations (Fig. 10 (b)) where

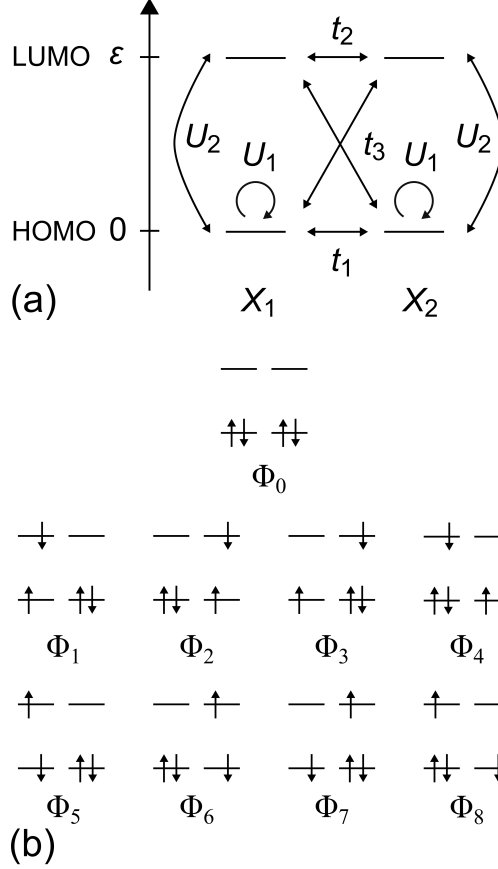


Figure 10: (a) Hubbard model of a system consisting of X_1 and X_2 . ϵ is the energy gap between the HOMO and LUMO. t_1 , t_2 , and t_3 are the hopping integrals for the HOMO-HOMO, LUMO-LUMO, and HOMO-LUMO, respectively, between X_1 and X_2 . U_1 and U_2 are the Coulomb interactions for the HOMO-HOMO and HOMO-LUMO, respectively, within X_1 or X_2 . (b) Electronic ground and excited configurations assuming a single excitation.

$|\Phi_0\rangle$ is the ground configuration, $|\Phi_1\rangle$, $|\Phi_2\rangle$, $|\Phi_5\rangle$, and $|\Phi_6\rangle$ are locally-excited configurations, and $|\Phi_3\rangle$, $|\Phi_4\rangle$, $|\Phi_7\rangle$, and $|\Phi_8\rangle$ are charge-transfer configurations. t_1 , t_2 , and t_3 are considered to be small compared with U_1 and U_2 because t_1 , t_2 , and t_3 are the interactions between X_1 and X_2 separated from each other while U_1 and U_2 are the interactions within X_1 or X_2 .

The model Hamiltonian for the basis defined in Fig. 10 (b) is given by

$$\begin{pmatrix} 2U_1 & 0 & 0 & t_3 & t_3 & 0 & 0 & t_3 & t_3 \\ \epsilon + U_1 + U_2 & 0 & t_2 & t_1 & 0 & 0 & 0 & 0 & 0 \\ \epsilon + U_1 + U_2 & t_1 & t_2 & 0 & 0 & 0 & 0 & 0 & 0 \\ \epsilon + U_1 + 2U_2 & 0 & 0 & 0 & 0 & 0 & 0 & 0 & 0 \\ \epsilon + U_1 + 2U_2 & 0 & 0 & 0 & 0 & 0 & 0 & 0 & 0 \\ \epsilon + U_1 + U_2 & 0 & t_2 & t_1 & 0 & 0 & 0 & 0 & 0 \\ \epsilon + U_1 + U_2 & t_1 & t_2 & 0 & 0 & 0 & 0 & 0 & 0 \\ \epsilon + U_1 + 2U_2 & 0 & 0 & 0 & 0 & 0 & 0 & 0 & 0 \\ \epsilon + U_1 + 2U_2 & 0 & 0 & 0 & 0 & 0 & 0 & 0 & 0 \end{pmatrix}. \quad (22)$$

Employing the Rayleigh–Schrödinger perturbation theory considering t_1 , t_2 , and t_3 as perturbations, the electronic states of the excited states are expressed as

$$\begin{aligned} |\Psi_1^s\rangle &= \frac{1}{2}(|\Phi_1\rangle + |\Phi_5\rangle + |\Phi_2\rangle + |\Phi_6\rangle) \\ &\quad - \frac{t_1 + t_2}{2U_2}(|\Phi_3\rangle + |\Phi_7\rangle + |\Phi_4\rangle + |\Phi_8\rangle), \end{aligned} \quad (23)$$

$$\begin{aligned} |\Psi_2^s\rangle &= \frac{1}{2}(|\Phi_3\rangle + |\Phi_7\rangle + |\Phi_4\rangle + |\Phi_8\rangle) \\ &\quad + \frac{t_1 + t_2}{2U_2}(|\Phi_1\rangle + |\Phi_5\rangle + |\Phi_2\rangle + |\Phi_6\rangle), \end{aligned} \quad (24)$$

$$\begin{aligned} |\Psi_1^a\rangle &= \frac{1}{2}(|\Phi_1\rangle + |\Phi_5\rangle - |\Phi_2\rangle - |\Phi_6\rangle) \\ &\quad - \frac{t_2 - t_1}{2U_2}(|\Phi_3\rangle + |\Phi_7\rangle - |\Phi_4\rangle - |\Phi_8\rangle), \end{aligned} \quad (25)$$

$$\begin{aligned} |\Psi_2^a\rangle &= \frac{1}{2}(|\Phi_3\rangle + |\Phi_7\rangle - |\Phi_4\rangle - |\Phi_8\rangle) \\ &\quad + \frac{t_2 - t_1}{2U_2}(|\Phi_1\rangle + |\Phi_5\rangle - |\Phi_2\rangle - |\Phi_6\rangle), \end{aligned} \quad (26)$$

where $|\Psi_1^s\rangle$ and $|\Psi_2^s\rangle$ are symmetric and $|\Psi_1^a\rangle$ and $|\Psi_2^a\rangle$ are antisymmetric electronic states. $|\Psi_1^s\rangle$ and $|\Psi_2^s\rangle$ belong to different symmetries from $|\Psi_1^a\rangle$ and $|\Psi_2^a\rangle$. The electronic states of the ground state is expressed as

$$|\Psi_0\rangle = |\Phi_0\rangle - \frac{t_3}{\epsilon - U_1 + U_2}(|\Phi_3\rangle + |\Phi_7\rangle + |\Phi_4\rangle + |\Phi_8\rangle), \quad (27)$$

which depends on t_3 unlike the electronic states of the excited states.

Employing the Rayleigh–Schrödinger perturbation theory, the energies of the ground and excited states are given by

$$E_0 = 2U_1 - \frac{4t_3^2}{\epsilon - U_1 + 2U_2}, \quad (28)$$

$$E_1^s = \epsilon + U_1 + U_2 - \frac{(t_1 + t_2)^2}{U_2}, \quad (29)$$

$$E_2^s = \epsilon + U_1 + 2U_2 + \frac{(t_1 + t_2)^2}{U_2}, \quad (30)$$

$$E_1^a = \epsilon + U_1 + U_2 - \frac{(t_2 - t_1)^2}{U_2}, \quad (31)$$

$$E_2^a = \epsilon + U_1 + 2U_2 + \frac{(t_2 - t_1)^2}{U_2}. \quad (32)$$

The energy difference between E_1^s and E_1^a as well as E_2^s and E_2^a is $|4t_1t_2/U_2|$. Since $4t_1t_2/U_2$ is assumed to be small, $|\Psi_1^s\rangle$ and $|\Psi_1^a\rangle$ as well as $|\Psi_2^s\rangle$ and $|\Psi_2^a\rangle$ are pseudo-degenerate. The orders of the excited states are $E_1^s \lesssim E_1^a < E_2^a \lesssim E_2^s$ for $t_1t_2 > 0$ and $E_1^a \lesssim E_1^s < E_2^s \lesssim E_2^a$ for $t_1t_2 < 0$: i.e. the symmetry of excited states changes according to the sign of the product t_1t_2 determined by the alignment of molecules. The excited state degenerates for $t_1t_2 = 0$. When t_1 , t_2 , and t_3 are no longer small compared to U_1 and U_2 , namely the perturbation theory is not valid, the degeneracy occurs in the case of $t_1 \neq 0$ or $t_2 \neq 0$ (see Fig. S10).

When the system has C_i symmetry and $t_1t_2 > 0$, S_1 is symmetry-forbidden A_g and S_2 is symmetry-allowed A_u . This is the case for Dimer Model **1** of the CNPPE solid. The electron density differences between S_1 ($|\Psi_1^s\rangle$) and S_0 ($|\Psi_0\rangle$) as well as S_2 ($|\Psi_1^a\rangle$) and S_0 are given by

$$\begin{aligned} \Delta\rho_{20} &= \Delta\rho_{10} \\ &= \{(|\phi_{\text{LU}}(X_1)|^2 - |\phi_{\text{HO}}(X_1)|^2) - (|\phi_{\text{LU}}(X_2)|^2 - |\phi_{\text{HO}}(X_2)|^2)\}. \end{aligned} \quad (33)$$

Thus, both $\Delta\rho_{20}$ and $\Delta\rho_{10}$ are expressed as the difference between the LUMOs and HOMOs

of X_1 and X_2 . In contrast, the electron density difference between S_2 and S_1 is expressed as

$$\Delta\rho_{21} = \Delta\rho_{20} - \Delta\rho_{10} = 0. \tag{34}$$

Therefore, $\Delta\rho_{21}$ is cancelled because $\Delta\rho_{20}$ and $\Delta\rho_{10}$ are the same due to the pseudo-degeneracy of S_1 and S_2 . The overlap density between S_2 and S_0 as well as between S_2 and S_1 are given by

$$\rho_{20} = \frac{1}{\sqrt{2}} (\phi_{\text{HO}}(X_1)\phi_{\text{LU}}(X_1) - \phi_{\text{HO}}(X_2)\phi_{\text{LU}}(X_2)), \tag{35}$$

$$\begin{aligned} \rho_{21} &= \frac{1}{2} \{ (|\phi_{\text{LU}}(X_1)|^2 - |\phi_{\text{HO}}(X_1)|^2) - (|\phi_{\text{LU}}(X_2)|^2 - |\phi_{\text{HO}}(X_2)|^2) \} \\ &\approx 0. \end{aligned} \tag{36}$$

ρ_{20} is expressed as the non-vanishing product of HOMOs and LUMOs. In contrast, ρ_{21} is cancelled because it is expressed as the difference between the square of the HOMOs and LUMOs. The other pairs of electron density differences and overlap densities in the pseudo-degenerate electronic system are summarized in Table S9 and Table S10, respectively.

Kasha originally discussed the spectroscopic properties of aggregates (H- and J-aggregations) using the long-range Coulomb couplings alone.[?] Spano *et al.* extended the Kasha's model by adding the short-range charge-transfer mediated excitonic couplings.^{??} This model explains that, when the short-range couplings, or intermolecular hopping integrals, are dominant, excited states properties are determined from the relative phases of the overlap between adjacent molecules, and the fluorescence could occur even in the H-aggregation. In the present system, however, the intermolecular hopping integrals are not dominant to apply the short-range coupling model.

Concluding remarks

The origin of AIEE in the CNPPE solid was investigated by the ONIOM method using the TD-DFT calculations. The pseudo-degeneracy arising from the excimer formation in the solid phase gives the vanished electron density difference and overlap density between S_1 and S_2 , which suggests that the fluorescence from the second excited state was possible against Kasha’s rule because the transitions from the second to first excited states are suppressed. The electronic states delocalized over the molecules reduce the diagonal VCCs in the solid phase to approximately $1/\sqrt{2}$ times those in solution phase. In addition, the packing effect in the solid phase reduces the off-diagonal VCCs of the intermolecular vibrations. These results indicate that the internal conversions from excited to ground states are more suppressed in the solid phase than in the solution phase. The molecular orientation affecting the relative signs of the intermolecular hopping integrals plays an important role in determining the pseudo-degenerate excited states properties. When the product of the hopping integrals for HOMOs and LUMOs is negative, the first excited state is fluorescent (J-type aggregation). In contrast, the product of the hopping integrals is positive, the first excited state is dark and the second one is fluorescent (H-type aggregation). Whether the first or second excited states are fluorescent, the AIEE could occur as long as the excimer forms in the aggregation phases because the excimer formation gives rise to the decrease of the diagonal VCCs.

In this study, we discussed a dimer with C_i site symmetry. Other cyano-substituted compounds exhibiting AIEE, such as cyano-substituted bis(4-bromophenyl)-fumaronitrile, bis(3-trifluoromethylphenyl)fumaronitrile, bis(4-methoxyphenyl)-fumaronitrile,³⁹ and cyano-substituted oligo(*para*-phenylene vinylene) (CN-DPDSB)⁴⁰ also have C_i site symmetry in their crystal structures, which suggests that AIEE may occur due to the pseudo-degeneracy in these compounds. It should be noted, however, that other symmetries including C_1 could be also possible for the appearance of AIEE if the pseudo-degenerate electronic states are generated in the aggregation phases.

A molecule which forms excimers with delocalized excited electronic states can be fluo-

rescent in the aggregation phases, even if the molecule is not fluorescent in an isolated state, such as in solution or vacuum. Accordingly, we can obtain the following design principle for AIEE: *a candidate molecule for AIEE should have pseudo-degenerate adiabatic electronic states in the aggregation phases originating from the excimer formation.*

Acknowledgement

This study was supported by JSPS KAKENHI Grant Number JP17H05259 in Scientific Research on Innovative Areas "Photosynergetics" and by Element Strategy Initiative of MEXT, Grant Number JPMXP0112101003. Numerical calculations were partly performed at Supercomputer System, Institute for Chemical Research, Kyoto University, Academic Center for Computing and Media Studies (ACCMS), Kyoto University, and Research Center for Computational Science, Okazaki.

Supporting Information Available

The following files are available free of charge.

References

- (1) Hong, Y.; Lam, J. W. Y.; Tang, B. Z. Aggregation-Induced Emission: Phenomenon, Mechanism and Applications. Chem. Commun. **2009**, 4332–4353.
- (2) Hong, Y.; Lam, J. W. Y.; Tang, B. Z. Aggregation-Induced Emission. Chem. Soc. Rev. **2011**, 40, 5361–5388.
- (3) Mei, J.; Hong, Y.; Lam, J. W. Y.; Qin, A.; Tang, Y.; Tang, B. Z. Aggregation-Induced Emission: the Whole is More Brilliant than the Parts. Adv. Mater. **2014**, 26, 5429–5479.

- (4) Chen, J.; Law, C. C. W.; Lam, J. W. Y.; Dong, Y.; Lo, S. M. F.; Williams, I. D.; Zhu, D.; Tang, B. Z. Synthesis, Light emission, Nanoaggregation, and Restricted Intramolecular Rotation of 1,1-Substituted 2,3,4,5-Tetraphenylsiloles. Chem. Mater. **2003**, 15, 1535–1546.
- (5) Yu, G.; Yin, S.; Liu, Y.; Chen, J.; Xu, X.; Sun, X.; Ma, D.; Zhan, X.; Peng, Q.; Shuai, Z.; Tang, B.; Zhu, D.; Fang, W.; Luo, Y. Structures, Electronic states, Photoluminescence, and Carrier Transport Properties of 1,1-Disubstituted 2,3,4,5-Tetraphenylsiloles. J. Am. Chem. Soc. **2005**, 127, 6335–6346.
- (6) Zhao, Z.; He, B.; Tang, B. Z. Aggregation-Induced Emission of Siloles. Chem. Sci. **2015**, 6, 5347–5365.
- (7) Zhang, T.; Jiang, Y.; Niu, Y.; Wang, D.; Peng, Q.; Shuai, Z. Aggregation Effects on the Optical Emission of 1,1,2,3,4,5-Hexaphenylsilole (HPS): a QM/MM Study. J. Phys. Chem. A **2014**, 118, 9094–9104.
- (8) Cornil, J.; Beljonne, D.; Calbert, J.-P.; Brédas, J.-L. Interchain Interactions in Organic π -Conjugated Materials: Impact on Electronic Structure, Optical Response, and Charge Transport. Adv. Mater. **2001**, 13, 1053–1067.
- (9) Rösch, U.; Yao, S.; Wortmann, R.; Würthner, F. Fluorescent H-aggregates of Merocyanine Dyes. Angew. Chem. **2006**, 118, 7184–7188.
- (10) Yoon, S.-J.; Chung, J. W.; Gierschner, J.; Kim, K. S.; Choi, M.-G.; Kim, D.; Park, S. Y. Multistimuli Two-Color Luminescence Switching via Different Slip-Stacking of Highly Fluorescent Molecular Sheets. J. Am. Chem. Soc. **2010**, 132, 13675–13683.
- (11) Yao, H.; Ashiba, K. Highly Fluorescent Organic Nanoparticles of Thiacyanine Dye: A Synergetic Effect of Intermolecular H-aggregation and Restricted Intramolecular Rotation. RSC Adv. **2011**, 1, 834–838.

- (12) Wang, L.; Shen, Y.; Yang, M.; Zhang, X.; Xu, W.; Zhu, Q.; Wu, J.; Tian, Y.; Zhou, H. Novel Highly Emissive H-aggregates with Aggregate Fluorescence Change in a Phenylbenzoxazole-Based System. Chem. Commun. **2014**, 50, 8723–8726.
- (13) Basak, S.; Nandi, N.; Bhattacharyya, K.; Datta, A.; Banerjee, A. Fluorescence from an H-aggregated Naphthalenediimide Based Peptide: Photophysical and Computational Investigation of This Rare Phenomenon. Phys. Chem. Chem. Phys. **2015**, 17, 30398–30403.
- (14) Lucenti, E.; Forni, A.; Botta, C.; Carlucci, L.; Giannini, C.; Marinotto, D.; Previtali, A.; Righetto, S.; Cariati, E. H-Aggregates Granting Crystallization-Induced Emissive Behavior and Ultralong Phosphorescence from a Pure Organic Molecule. J. Phys. Chem. Lett. **2017**, 8, 1894–1898.
- (15) Qian, H.; Cousins, M. E.; Horak, E. H.; Wakefield, A.; Liptak, M. D.; Aprahamian, I. Suppression of Kasha’s Rule as a Mechanism for Fluorescent Molecular Rotors and Aggregation-Induced Emission. Nat. Chem. **2017**, 9, 83.
- (16) Ryu, N.; Okazaki, Y.; Pouget, E.; Takafuji, M.; Nagaoka, S.; Ihara, H.; Oda, R. Fluorescence Emission Originated from the H-aggregated Cyanine Dye with Chiral Gemini Surfactant Assemblies Having a Narrow Absorption Band and a Remarkably Large Stokes Shift. Chem. Commun. **2017**, 53, 8870–8873.
- (17) Kasha, M. Characterization of Electronic Transitions in Complex Molecules. Disc. Faraday Soc. **1950**, 9, 14–19.
- (18) Sato, T. Fluorescence via Reverse Intersystem Crossing from Higher Triplet States. J. Comput. Chem. Jpn. **2016**, 14, 189–192.
- (19) Sato, T.; Hayashi, R.; Haruta, N.; Pu, Y.-J. Fluorescence via Reverse Intersystem Crossing from Higher Triplet States in a Bisanthracene Derivative. Sci. Rep. **2017**, 7, 4820.

- (20) Pu, Y.-J.; Satake, R.; Koyama, Y.; Otomo, T.; Hayashi, R.; Haruta, N.; Katagiri, H.; Otsuki, D.; Kim, D.; Sato, T. Absence of Delayed Fluorescence and Triplet–Triplet Annihilation in Organic Light Emitting Diodes with Spatially Orthogonal BIANTRACENES. J. Mater. Chem. C **2019**, 7, 2541–2547.
- (21) Endo, A.; Ogasawara, M.; Takahashi, A.; Yokoyama, D.; Kato, Y.; Adachi, C. Thermally activated delayed fluorescence from Sn⁴⁺–porphyrin complexes and their application to organic light emitting diodes—A novel mechanism for electroluminescence. Adv. Mater. **2009**, 21, 4802–4806.
- (22) Adachi, C. Third-Generation Organic Electroluminescence Materials. Jpn. J. Appl. Phys. **2014**, 53, 060101.
- (23) Hu, J.-Y.; Pu, Y.-J.; Satoh, F.; Kawata, S.; Katagiri, H.; Sasabe, H.; Kido, J. Bisanthracene-Based Donor–Acceptor-type Light-Emitting Dopants: Highly Efficient Deep-Blue Emission in Organic Light-Emitting Devices. Adv. Funct. Mater. **2014**, 24, 2064–2071.
- (24) Nishio, S.; Higashiguchi, K.; Matsuda, K. The Effect of Cyano Substitution on the Fluorescence Behavior of 1,2-Bis(pyridylphenyl)ethene. Asian J. Org. Chem. **2014**, 3, 686–690.
- (25) Shizu, K.; Sato, T.; Tanaka, K. Inverse Relationship of Reorganization Energy to The Number of π Electrons from Perspective of Vibronic Coupling Density. J. Comput. Chem. Jpn. **2013**, 12, 215–221.
- (26) Sato, T.; Tokunaga, K.; Tanaka, K. Vibronic Coupling in Naphthalene Anion: Vibronic Coupling Density Analysis for Totally Symmetric Vibrational Modes. J. Phys. Chem. A **2008**, 112, 758–767.
- (27) Sato, T.; Tokunaga, K.; Iwahara, N.; Shizu, K.; Tanaka, K. Vibronic Coupling Constant and Vibronic Coupling Density. In The Jahn-Teller Effect: Fundamentals and

- Implications for Physics and Chemistry; Köppel, H., Yarkony, D. R., Barentzen, H., Eds.; Springer-Verlag: Berlin and Heidelberg, 2009; pp 99–129.
- (28) Sato, T.; Uejima, M.; Iwahara, N.; Haruta, N.; Shizu, K.; Tanaka, K. Vibronic Coupling Density and Related Concepts. J. Phys.: Conf. Ser. **2013**, 428, 012010.
- (29) Fischer, G. Vibronic Coupling: The Interaction between the Electronic and Nuclear Motions; Academic Press: London, 1984.
- (30) Azumi, T.; Matsuzaki, K. What Does the Term "Vibronic Coupling" Mean? Photochem. Photobiol. **1977**, 25, 315–326.
- (31) Uejima, M.; Sato, T.; Yokoyama, D.; Tanaka, K.; Park, J.-W. Quantum Yield in Blue-Emitting Anthracene Derivatives: Vibronic Coupling Density and Transition Dipole Moment Density. Phys. Chem. Chem. Phys. **2014**, 16, 14244–14256.
- (32) Hutchisson, E. Band spectra intensities for symmetrical diatomic molecules. Phys. Rev. **1930**, 36, 410.
- (33) Svensson, M.; Humbel, S.; Froese, R. D.; Matsubara, T.; Sieber, S.; Morokuma, K. ONIOM: a multilayered integrated MO+ MM method for geometry optimizations and single point energy predictions. A test for Diels- Alder reactions and Pt (P (t-Bu) 3) 2+ H2 oxidative addition. J. Phys. Chem. **1996**, 100, 19357–19363.
- (34) Chung, L. W.; Sameera, W.; Ramozzi, R.; Page, A. J.; Hatanaka, M.; Petrova, G. P.; Harris, T. V.; Li, X.; Ke, Z.; Liu, F.; Li, H.-B.; Ding, L.; Morokuma, K. The ONIOM Method and its Applications. Chem. Rev. **2015**, 115, 5678–5796.
- (35) Tomasi, J.; Mennucci, B.; Cammi, R. Quantum mechanical continuum solvation models. Chem. Rev. **2005**, 105, 2999–3094.
- (36) Frisch, M. J.; Trucks, G. W.; Schlegel, H. B.; Scuseria, G. E.; Robb, M. A.; Cheeseman, J. R.; Scalmani, G.; Barone, V.; Mennucci, B.; Petersson, G. A.; Nakatsuji, H.;

Caricato, M.; Li, X.; Hratchian, H. P.; Izmaylov, A. F.; Bloino, J.; Zheng, G.; Sonnenberg, J. L.; Hada, M.; Ehara, M.; Toyota, K.; Fukuda, R.; Hasegawa, J.; Ishida, M.; Nakajima, T.; Honda, Y.; Kitao, O.; Nakai, H.; Vreven, T.; Montgomery Jr., J. A.; Peralta, J. E.; Ogliaro, F.; Bearpark, B.; J, H. J.; Brothers, E.; Kudin, K. N.; Staroverov, V. N.; Keith, T.; Kobayashi, R.; Normand, J.; Raghavachari, K.; Rendell, A.; Burant, J. C.; Iyengar, S. S.; Tomasi, J.; Cossi, M.; Rega, N.; Millam, J. M.; Klene, M.; Knox, J. E.; Cross, J. B.; Bakken, V.; Adamo, C.; Jaramillo, J.; Gomperts, R.; Stratmann, R. E.; Yazyev, O.; Austin, A. J.; Cammi, R.; Pomelli, C.; Ochterski, J. W.; Martin, R. L.; Morokuma, K.; Zakrzewski, V. G.; Voth, G. A.; Salvador, P.; Dannenberg, J. J.; Dapprich, S.; Daniels, A. D.; Farkas, O.; Foresman, J. B.; Ortiz, J. V.; Cioslowski, J.; Fox, D. J. Gaussian 09, Revision D. 01, Gaussian, Inc.: Wallingford, CT, 2013.

- (37) Frisch, M. J.; Trucks, G. W.; Schlegel, H. B.; Scuseria, G. E.; Robb, M. A.; Cheeseman, J. R.; Scalmani, G.; Barone, V.; Mennucci, B.; Petersson, G. A.; Nakatsuji, H.; Caricato, M.; Li, X.; Hratchian, H. P.; Izmaylov, A. F.; Bloino, J.; Zheng, G.; Sonnenberg, J. L.; Hada, M.; Ehara, M.; Toyota, K.; Fukuda, R.; Hasegawa, J.; Ishida, M.; Nakajima, T.; Honda, Y.; Kitao, O.; Nakai, H.; Vreven, T.; Montgomery Jr., J. A.; Peralta, J. E.; Ogliaro, F.; Bearpark, B.; J, H. J.; Brothers, E.; Kudin, K. N.; Staroverov, V. N.; Keith, T.; Kobayashi, R.; Normand, J.; Raghavachari, K.; Rendell, A.; Burant, J. C.; Iyengar, S. S.; Tomasi, J.; Cossi, M.; Rega, N.; Millam, J. M.; Klene, M.; Knox, J. E.; Cross, J. B.; Bakken, V.; Adamo, C.; Jaramillo, J.; Gomperts, R.; Stratmann, R. E.; Yazyev, O.; Austin, A. J.; Cammi, R.; Pomelli, C.; Ochterski, J. W.; Martin, R. L.; Morokuma, K.; Zakrzewski, V. G.; Voth, G. A.; Salvador, P.; Dannenberg, J. J.; Dapprich, S.; Daniels, A. D.; Farkas, O.; Foresman, J. B.; Ortiz, J. V.; Cioslowski, J.; Fox, D. J. Gaussian 09, Revision E. 01, Gaussian, Inc.: Wallingford, CT, 2013.

- (38) Sato, T.; Iwahara, N.; Haruta, N.; Tanaka, K. C₆₀ bearing ethylene moieties. Chem. Phys. Lett. **2012**, 531, 257–260.
- (39) Yeh, H.-C.; Wu, W.-C.; Wen, Y.-S.; Dai, D.-C.; Wang, J.-K.; Chen, C.-T. Derivative of α , β -Dicyanostilbene: Convenient Precursor for the Synthesis of Diphenylmaleimide Compounds, E-Z Isomerization, Crystal Structure, and Solid-State Fluorescence. J. Org. Chem. **2004**, 69, 6455–6462.
- (40) Li, Y.; Li, F.; Zhang, H.; Xie, Z.; Xie, W.; Xu, H.; Li, B.; Shen, F.; Ye, L.; Hanif, M.; Ma, D.; Ma, Y. Tight Intermolecular Packing through Supramolecular Interactions in Crystals of Cyano Substituted Oligo(para-phenylene Vinylene): a Key Factor for Aggregation-Induced Emission. Chem. Commun. **2007**, 231–233.

Supplementary Information

Origin of Aggregation-Induced Enhanced Emission: Role of Pseudo-Degenerate Electronic States of Excimers Formed in Aggregation Phases

Wataru Ota,^{a,b} Ken Takahashi,^c Kenji Higashiguchi,^d

Kenji Matsuda,^d and Tohru Sato,^{*a,b,e}

April 14, 2020

^a Fukui Institute for Fundamental Chemistry, Kyoto University, Sakyo-ku, Kyoto 606-8103, Japan;

^b Department of Molecular Engineering, Graduate School of Engineering, Kyoto University, Nishikyo-ku, Kyoto 615-8510, Japan

^c Undergraduate School of Industrial Chemistry, Faculty of Engineering, Kyoto University, Nishikyo-ku, Kyoto 615-8510, Japan

^d Department of Synthetic Chemistry and Biological Chemistry, Kyoto University, Nishikyo-ku, Kyoto 615-8510, Japan

^e Unit of Elements Strategy Initiative for Catalysts & Batteries, Kyoto University, Nishikyo-ku, Kyoto 615-8510, Japan

E-mail: tsato@scl.kyoto-u.ac.jp

Contents

S1 Dimer Models in Solid Phase	3
S2 Irreducible Representations of Excimers	4
S2.1 C_i symmetry	4
S2.2 C_2 symmetry	5
S2.3 C_s symmetry	6
S3 Rate Constant of Internal Conversion for Monomer Model and Dimer Model 1	7
S4 Electron Density Differences of Dimer Model 2 and 3	8
S5 Potential Derivatives of Monomer Model and Dimer Model 1	9
S6 Potential Energy Surface of Monomer Model	10
S7 Decamer Model in Solid Phase	11
S8 Dimer Model 1 Calculated by ωB97X-D Functional	13
S9 Hubbard Model of a Pseudo-Degenerate Electronic System	14

S1 Dimer Models in Solid Phase

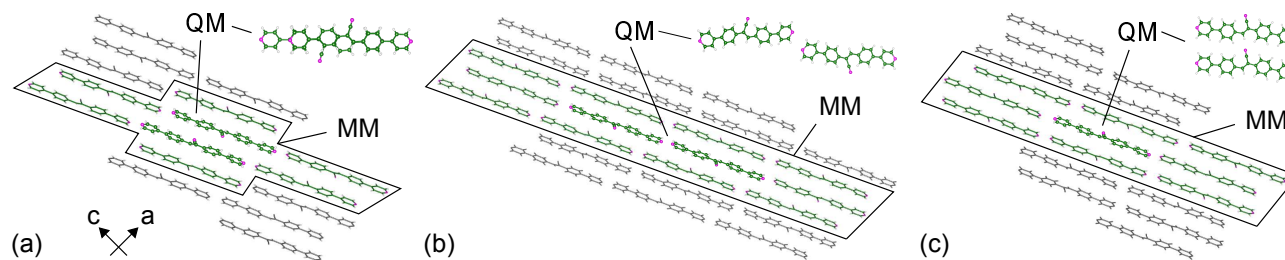


Fig. S1 Dimer Model (a) **1**, (b) **2**, and (c) **3** for the CNPPE solid. In Dimer Model **2**, a dimer aligned in the *ca*-plane was selected as the QM region and the surrounding 38 molecules were selected as the MM region. In Dimer Model **3**, a dimer aligned in the *b*-direction was selected as the QM region and the surrounding 29 molecules were selected as the MM region. The QM region was computed at the M06-2X/6-31G(d,p) levels of theory and the MM region was computed using the UFF.

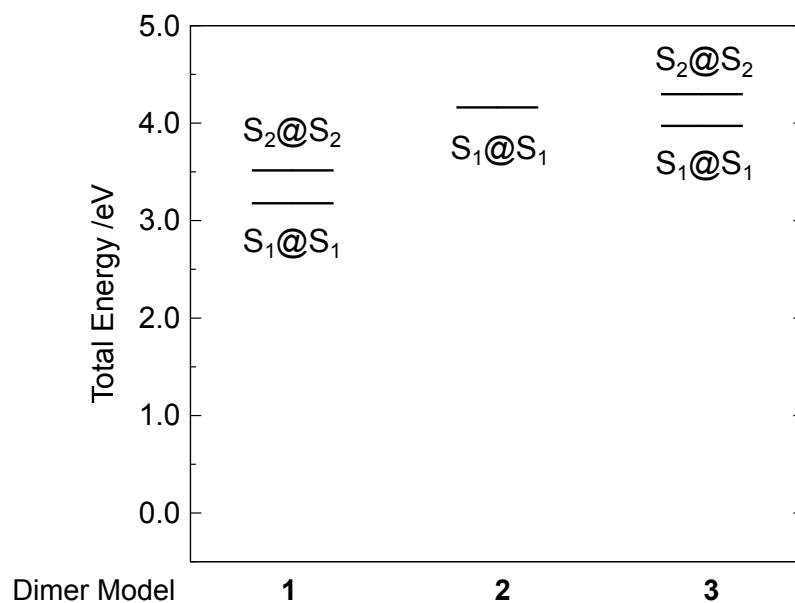


Fig. S2 Total energy of the excited states of Dimer Model **1**, **2**, and **3** in the QM region. The energy reference is the total energy of S₀@S₀ of Dimer Model **1**, -2253.41783105 a.u.

S2 Irreducible Representations of Excimers

S2.1 C_i symmetry

Table S1 presents the character table of C_i point group¹. In C_i point group, there are cases where an atom does not exist at the inversion center and where an atom exists at the inversion center. When an atom does not exist at the inversion center, the reducible representation of vibrational modes is decomposed as

$$\Gamma_{\text{vib}} = \frac{3N-6}{2}A_g + \frac{3N-6}{2}A_u, \quad (1)$$

where N denotes the number of atoms. Half of the vibrational modes belongs to A_g and the other half to A_u .

On the other hand, when an atom exists at the inversion center, the number of vibrational modes is

$$\Gamma_{\text{vib}} = \frac{3N-9}{2}A_g + \frac{3N-3}{2}A_u. \quad (2)$$

The numbers of vibrational modes belonging to A_g and A_u are different.

Table S1 Character table of C_i point group.

C_i	E	i	$h=2$
A_g	1	1	R_x, R_y, R_z $x^2, y^2, z^2, xy, yz, zx$
A_u	1	-1	x, y, z

S2.2 C_2 symmetry

Table S2 presents the character table of C_2 point group¹. In C_2 point group, there are cases where no atoms exist on a rotational axis and where atoms exist on a rotational axis. When atoms do not exist on a rotational axis, the reducible representation of vibrational modes is decomposed as

$$\Gamma_{\text{vib}} = \frac{3N-4}{2}A + \frac{3N-8}{2}B. \quad (3)$$

The numbers of vibrational modes belonging to A and B are not the same. When N_a atoms exist on a rotational axis, the number of vibrational modes is

$$\Gamma_{\text{vib}} = \frac{3N-N_a-4}{2}A + \frac{3N+N_a-8}{2}B. \quad (4)$$

The number of vibrational modes belonging to B increases with N_a .

Table S2 Character table of C_2 point group.

C_2	E	C_2		$h=2$
A	1	1	z, R_z	x^2, y^2, z^2, xy
B	1	-1	x, y, R_x, R_y	yz, zx

S2.3 C_s symmetry

Table S3 presents the character table of C_s point group¹. In C_s point group, there are cases where no atoms exist on a mirror plane and where atoms exist on a mirror plane. When atoms do not exist on a mirror plane, the reducible representation of vibrational modes is decomposed as

$$\Gamma_{\text{vib}} = \frac{3N-6}{2}A' + \frac{3N-6}{2}A'' \quad (5)$$

Half of the vibrational modes belongs to A' and the other half to A'' . When N_p atoms exist on a mirror plane, the number of vibrational modes is

$$\Gamma_{\text{vib}} = \frac{3N+N_p-6}{2}A' + \frac{3N-N_p-6}{2}A'' \quad (6)$$

The number of vibrational modes belonging to A' increases with N_p .

Table S3 Character table of C_s point group.

C_s	E	σ_h	$h=2$	
A'	1	1	x, y, R_z	x^2, y^2, z^2, xy
A''	1	-1	z, R_x, R_y	yz, zx

S3 Rate Constant of Internal Conversion for Monomer Model and Dimer Model

1

Table S4 Dependence of $k_{n\leftarrow m}^{\text{IC}}(T)$ within a single mode approximation on the linewidth of the Gaussian function σ . $V_{mn,\alpha} = 5 \times 10^{-4}$ a.u., $\omega_\alpha = 1700 \text{ cm}^{-1}$, $E_m - E_n = 3.0 \text{ eV}$, $E_{\text{min}} = -11500 \text{ cm}^{-1}$, and $E_{\text{max}} = 11500 \text{ cm}^{-1}$. $V_{n,\alpha}$ at maximum coupling mode of Monomer model is 8.42×10^{-4} a.u. and of Dimer Model **1** is 5.27×10^{-4} a.u. Ratios of $k_{n\leftarrow m}^{\text{IC}}(T)$ of Monomer Model to Dimer Model **1** are also given.

$\sigma \text{ (cm}^{-1}\text{)}$	$k_{n\leftarrow m}^{\text{IC}} \text{ (s}^{-1}\text{)}$		Ratio
	Monomer Model	Dimer Model 1	
300	1.195×10^{10}	2.998×10^7	388
400	1.335×10^{10}	3.985×10^7	335
500	1.569×10^{10}	5.651×10^7	277
600	1.832×10^{10}	7.552×10^7	242
700	2.092×10^{10}	9.525×10^7	219

S4 Electron Density Differences of Dimer Model 2 and 3

Table S5 Excited states of Dimer Model 2 at the S_0 and S_1 optimized structures.

State	Excitation Energy		f	Major Configuration (CI Coefficient)
	eV	nm		
@ S_0 S_1 (A)	3.8692	320.44	3.2829	HO-1 \rightarrow LU (0.398), HO \rightarrow LU+1 (0.565)
S_2 (A)	3.9294	315.53	0.0977	HO-1 \rightarrow LU (0.565), HO \rightarrow LU+1 (-0.399)
@ S_1 S_1 (A)	3.1122	398.39	1.8360	HO \rightarrow LU (0.700)
S_2 (A)	3.9107	317.04	1.5560	HO-1 \rightarrow LU+1 (0.791)

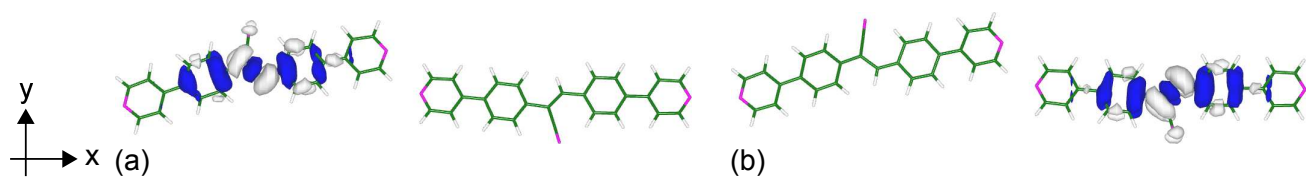


Fig. S3 Electron density differences of (a) S_1 @ S_1 - S_0 @ S_1 and (b) S_2 @ S_1 - S_0 @ S_1 for Dimer Model 2. Isosurface values are 1.0×10^{-3} a.u.

Table S6 Excited states of Dimer Model 3 at the S_0 and S_2 optimized structures.

State	Excitation Energy		f	Major Configuration (CI Coefficient)
	eV	nm		
@ S_0 S_1 (A)	3.7862	327.46	0.1146	HO-1 \rightarrow LU (0.57769), HO \rightarrow LU+1 (-0.37639)
S_2 (A)	3.9346	315.12	2.6588	HO-1 \rightarrow LU (0.38099), HO \rightarrow LU+1 (0.57373)
@ S_2 S_1 (A)	3.3696	367.95	0.0005	HO-1 \rightarrow LU (0.49586), HO \rightarrow LU+1 (-0.48388)
S_2 (A)	3.5310	351.13	2.8119	HO-1 \rightarrow LU (0.48848), HO \rightarrow LU+1 (0.49548)

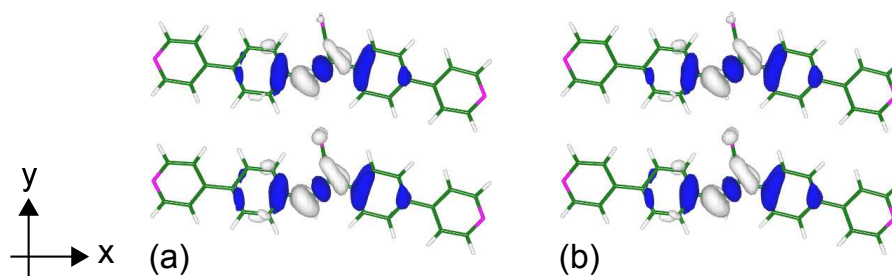


Fig. S4 Electron density differences of (a) S_1 @ S_2 - S_0 @ S_2 and (b) S_2 @ S_2 - S_0 @ S_2 for Dimer Model 3. Isosurface values are 1.0×10^{-3} a.u.

S5 Potential Derivatives of Monomer Model and Dimer Model 1

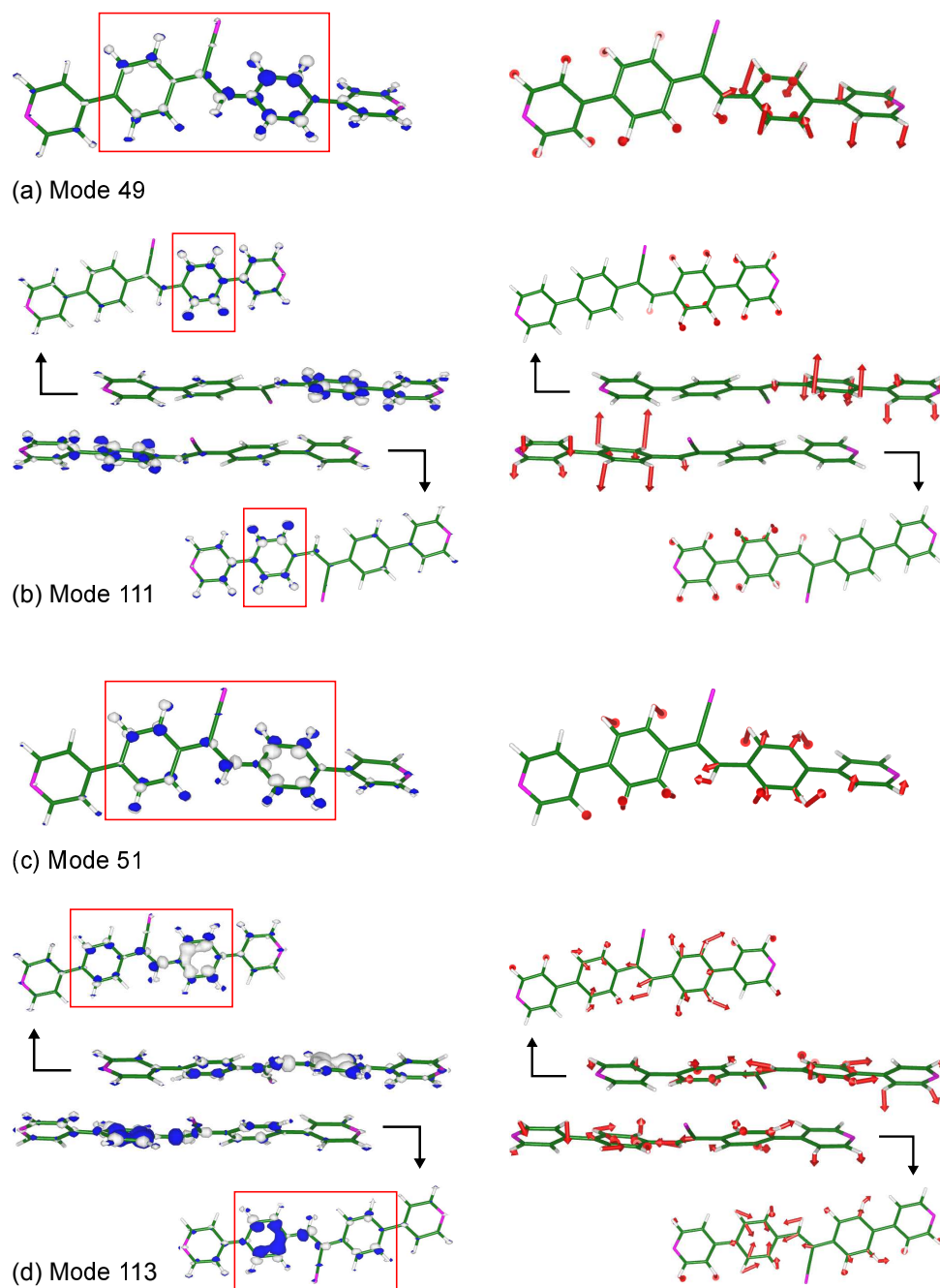


Fig. S5 Potential derivatives of (a) mode 49 for Monomer Model and (b) mode 111 for Dimer Model **1** of which the off-diagonal VCC is reduced by the packing effect. Potential derivatives of (c) mode 51 for Monomer Model and (d) mode 113 for Dimer Model **1** of which the off-diagonal VCC is not reduced by the packing effect. Isosurface value for Monomer Model is 1×10^{-2} a.u. and for Dimer Model **1** is $1/\sqrt{2} \times 10^{-2}$ a.u.

S6 Potential Energy Surface of Monomer Model

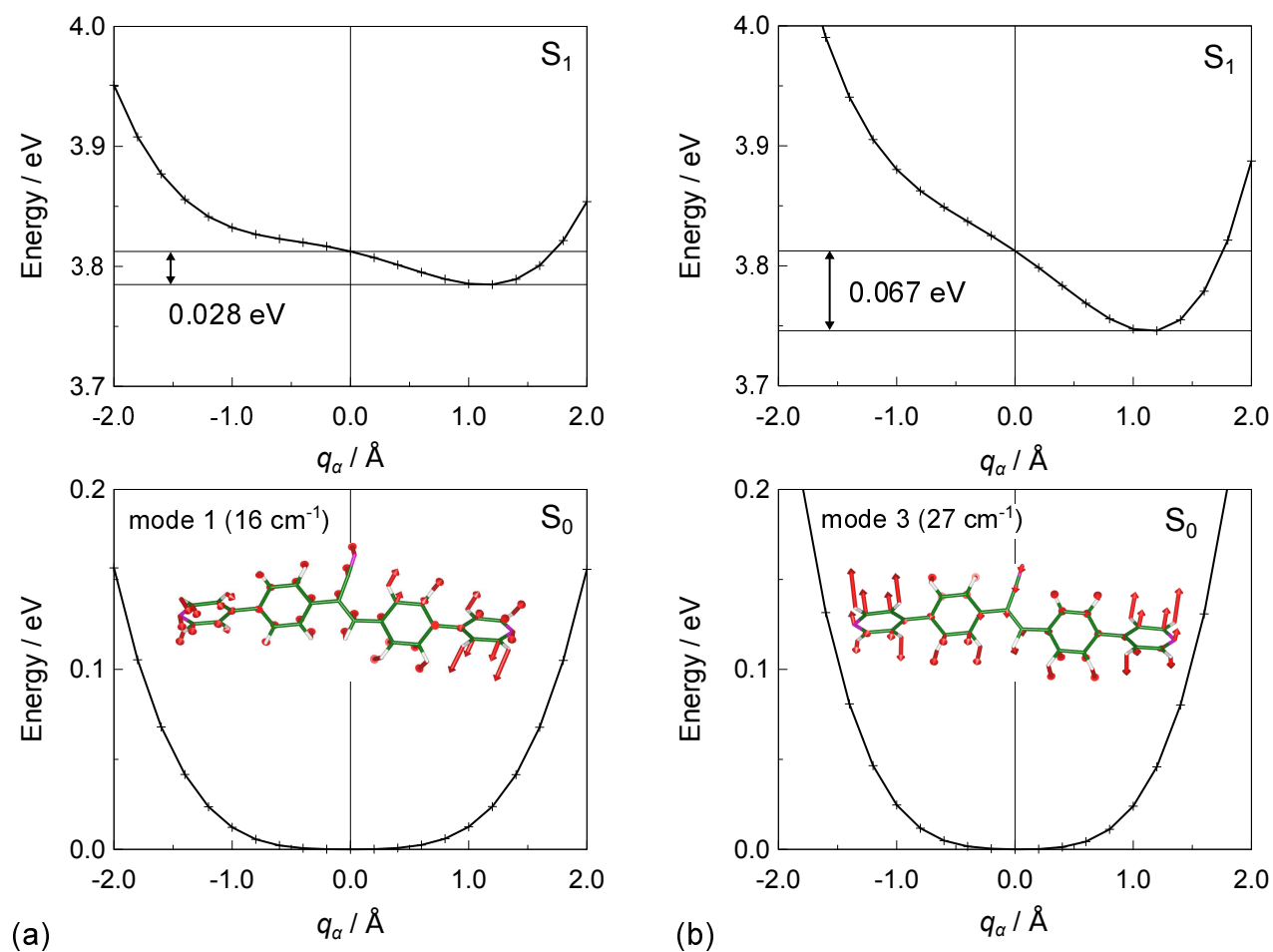


Fig. S6 Potential energy surfaces of S_0 and S_1 of Monomer Model along with (a) mode 1 and (b) mode 3. q_α denotes the Cartesian displacement from the S_0 optimized structure. The potential energy surfaces along with these modes were not approximated to harmonic potentials. The reorganization energies of modes 1 and 3 including the anharmonicity effect were calculated to be 0.028 and 0.067 eV, respectively.

S7 Decamer Model in Solid Phase

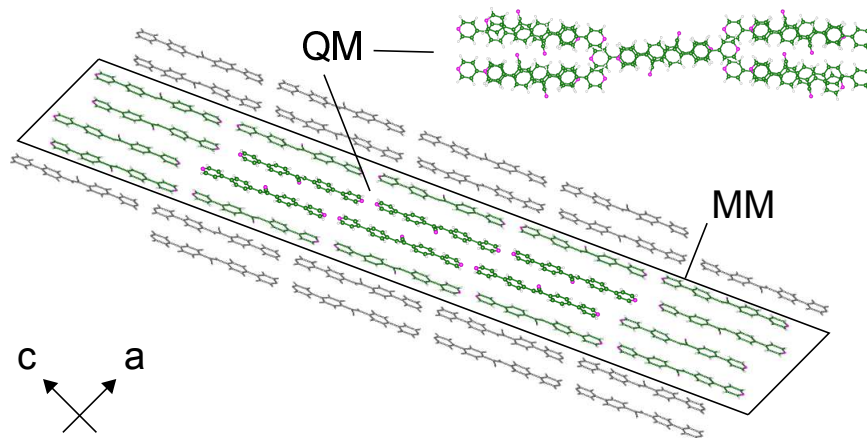


Fig. S7 Decamer Model for the CNPPE solid. Centered decamer is selected as the QM region (M06-2X/3-21G) and the surrounding 60 molecules are selected as the MM region (UFF).

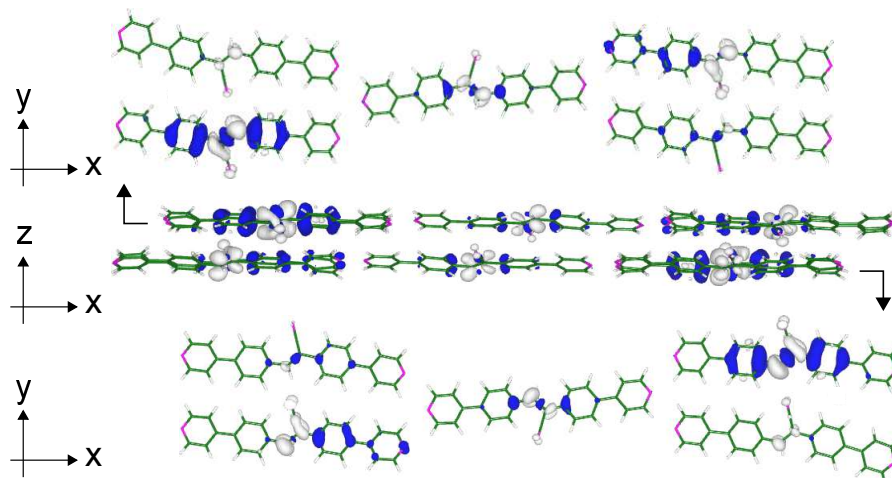


Fig. S8 Electron density difference of $S_8@S_0-S_0@S_0$ for Decamer Model. Isosurface value is 3.0×10^{-4} a.u.

Table S7 Excited states of Decamer Model at the S_0 optimized structure.

State	Excitation Energy		f	Major Configuration (CI Coefficient)
	eV	nm		
$S_1 (A_u)$	3.7447	331.09	0.0052	HO-4 \rightarrow LU (0.2715), HO-4 \rightarrow LU+5 (-0.2389) HO-3 \rightarrow LU+1 (-0.2715), HO-3 \rightarrow LU+4 (-0.2389)
$S_2 (A_g)$	3.7447	331.09	0.0000	HO-4 \rightarrow LU+1 (0.2717), HO-4 \rightarrow LU+4 (0.2392) HO-3 \rightarrow LU (-0.2717), HO-3 \rightarrow LU+5 (0.2392)
$S_3 (A_g)$	3.7775	328.21	0.0000	HO-4 \rightarrow LU+1 (0.2197), HO-3 \rightarrow LU (-0.2199) HO-2 \rightarrow LU+3 (0.2583), HO-1 \rightarrow LU+2 (0.2583)
$S_4 (A_u)$	3.7775	328.21	0.0618	HO-4 \rightarrow LU (-0.2204), HO-3 \rightarrow LU+1 (0.2204) HO-2 \rightarrow LU+2 (0.2580), HO-1 \rightarrow LU+3 (0.2580)
$S_5 (A_u)$	3.8860	319.06	0.7377	HO-4 \rightarrow LU+2 (-0.2070), HO-4 \rightarrow LU+5 (0.2771) HO-3 \rightarrow LU+3 (-0.2070), HO-3 \rightarrow LU+4 (0.2771) HO-2 \rightarrow LU+6 (-0.2052), HO-1 \rightarrow LU+7 (0.2052)
$S_6 (A_g)$	3.8871	318.96	0.0000	HO-4 \rightarrow LU+3 (-0.2030), HO-4 \rightarrow LU+4 (0.2690) HO-3 \rightarrow LU+2 (-0.2030), HO-3 \rightarrow LU+5 (0.2690) HO-2 \rightarrow LU+7 (0.2208), HO-1 \rightarrow LU+6 (-0.2208)
$S_7 (A_g)$	3.9259	315.81	0.0000	HO-5 \rightarrow LU+9 (-0.2354), HO \rightarrow LU+8 (0.6484)
$S_8 (A_u)$	3.9942	310.41	9.0385	HO-2 \rightarrow LU+6 (-0.3474), HO-1 \rightarrow LU+7 (0.3474) HO \rightarrow LU+9 (-0.2498)
$S_9 (A_g)$	4.0290	307.73	0.0000	HO-2 \rightarrow LU+7 (-0.3649), HO-1 \rightarrow LU+6 (0.3649)
$S_{10} (A_u)$	4.1224	300.76	1.1521	HO \rightarrow LU+9 (-0.5282)

S8 Dimer Model 1 Calculated by ω B97X-D Functional

Table S8 Excited states of Dimer Model 1 at the S_0 and S_2 optimized structures calculated by ω B97X-D/6-31G(d,p) level of theory. f denotes the oscillator strength.

State	Excitation Energy			Major Configuration (CI coefficient)
	eV	nm	f	
@ S_0 $S_1(A_g)$	3.8193	324.63	0.0000	HO-1 \rightarrow LU+1 (-0.379) HO \rightarrow LU (0.564)
$S_2(A_u)$	3.9453	314.26	2.3698	HO-1 \rightarrow LU (-0.406) HO \rightarrow LU+1 (0.542)
@ S_2 $S_1(A_g)$	3.3319	372.12	0.0000	HO-1 \rightarrow LU+1 (0.347) HO \rightarrow LU (0.592)
$S_2(A_u)$	3.4697	357.33	2.3091	HO-1 \rightarrow LU (0.379) HO \rightarrow LU+1 (0.570)

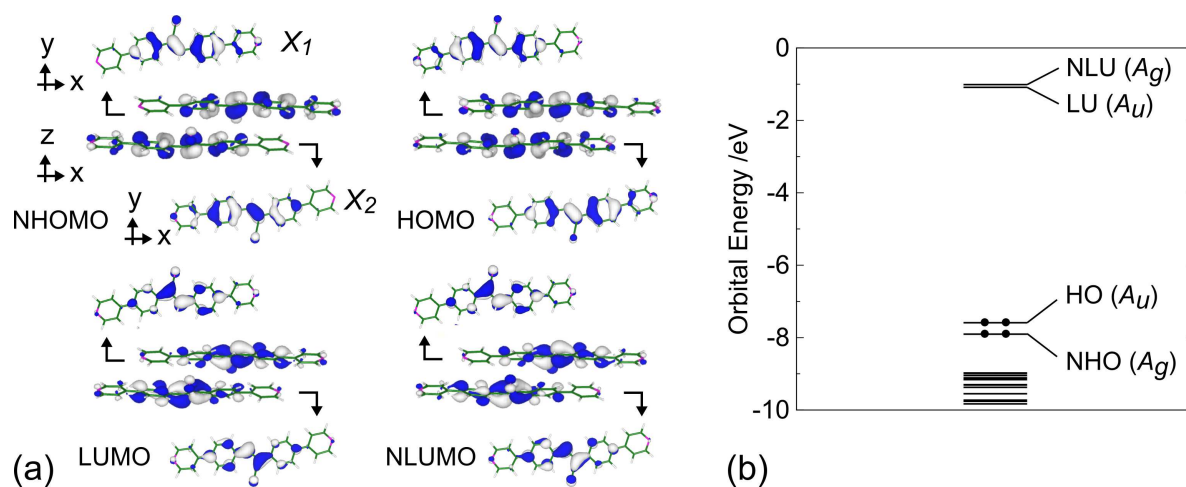


Fig. S9 (a) Frontier orbitals and (b) orbital levels of Dimer Model 1 at the S_2 optimized structure calculated by ω B97X-D/6-31G(d,p) level of theory. X_1 and X_2 are the constituent molecules of Dimer Model 1. Isosurface values of the frontier orbitals are 3.0×10^{-2} a.u.

S9 Hubbard Model of a Pseudo-Degenerate Electronic System

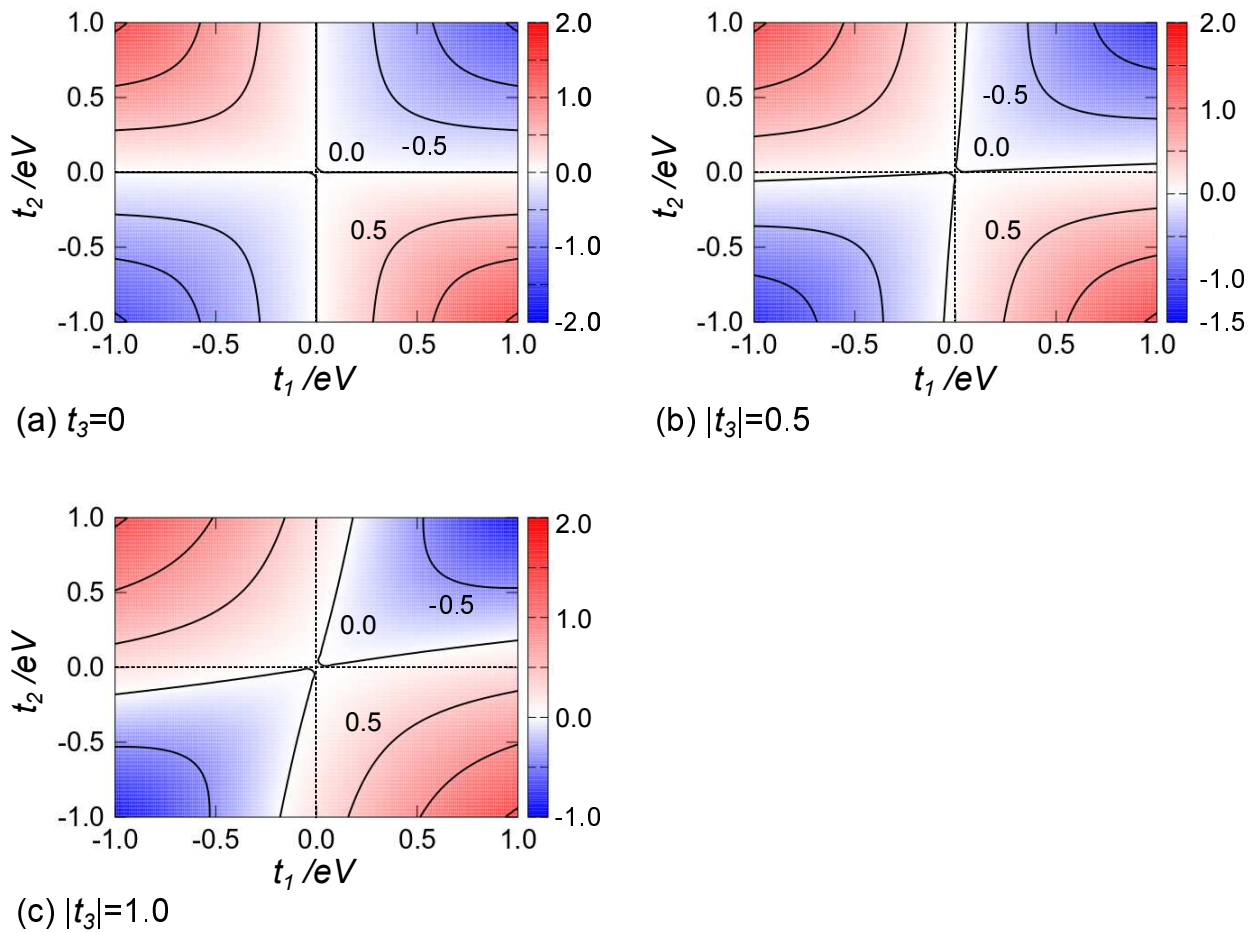


Fig. S10 Energy difference between first and second excited states, $E_1^s - E_1^a$, calculated by numerically diagonalizing the Hubbard Hamiltonian. ε , U_1 , and U_2 were set to 3.0, 1.0, and 1.0, respectively.

In this section, we describe the electron density differences and overlap densities in the pseudo-degenerate electronic system using the Hubbard model. The electron density in the ground state is defined by ρ_0 . The orbital overlap densities are defined by

$$p_1 = |\phi_{\text{HO}}(X_1)|^2, \quad p_2 = |\phi_{\text{HO}}(X_2)|^2, \quad q_1 = |\phi_{\text{LU}}(X_1)|^2, \quad q_2 = |\phi_{\text{LU}}(X_2)|^2, \quad (7)$$

$$r_1 = \phi_{\text{HO}}(X_1)\phi_{\text{LU}}(X_1), \quad r_2 = \phi_{\text{HO}}(X_2)\phi_{\text{LU}}(X_2), \quad (8)$$

$$s_1 = \phi_{\text{HO}}(X_1)\phi_{\text{HO}}(X_2), \quad s_2 = \phi_{\text{LU}}(X_1)\phi_{\text{LU}}(X_2), \quad s_3 = \phi_{\text{HO}}(X_1)\phi_{\text{LU}}(X_2) = \phi_{\text{LU}}(X_1)\phi_{\text{HO}}(X_2), \quad (9)$$

where $\phi_{\text{HO/LU}}(X_1/X_2)$ represent the HOMO/LUMO of X_1/X_2 . The overlaps between X_1 and X_2 separated from each other, namely s_1 , s_2 and s_3 , are supposed to be 0. Table S9 and S10 respectively present the electron density differences and overlap densities in the pseudo-degenerate electronic system.

Table S9 Electron density differences in the pseudo-degenerate system. $\alpha = \frac{1}{2}((\rho_0 - p_1 + q_1) + (\rho_0 - p_2 + q_2))$. For Dimer Model 1 of the CNPPE solid, S_1 corresponds to $|\Psi_1^s\rangle$, and S_2 $|\Psi_1^a\rangle$. Therefore, the electron density difference between S_1 and S_2 is given by 0.

	Ψ_0	Ψ_1^s	Ψ_2^s	Ψ_1^a	Ψ_2^a
Ψ_0	0	$\rho_0 - \alpha$	$\rho_0 - \alpha$	$\rho_0 - \alpha$	$\rho_0 - \alpha$
Ψ_1^s		0	0	0	0
Ψ_2^s			0	0	0
Ψ_1^a				0	0
Ψ_2^a					0

Table S10 Overlap densities in the pseudo-degenerate system. $\alpha = \frac{1}{2}((\rho_0 - p_1 + q_1) + (\rho_0 - p_2 + q_2))$, $\beta_1 = \frac{1}{2}(q_1 - p_1 - q_2 + p_2) \approx 0$, $\beta_2 = \frac{1}{2}(q_2 - p_1 - q_1 + p_2)$, $\gamma_1 = \frac{1}{\sqrt{2}}(r_1 + r_2)$, $\gamma_2 = \frac{1}{\sqrt{2}}(r_1 - r_2)$. For Dimer Model 1 of the CNPPE solid, S_1 corresponds to $|\Psi_1^s\rangle$, and S_2 $|\Psi_1^a\rangle$. Therefore, the overlap density between S_1 and S_2 is given by $\beta_1 \approx 0$.

	Ψ_0	Ψ_1^s	Ψ_2^s	Ψ_1^a	Ψ_2^a
Ψ_0	ρ_0	γ_1	$\frac{t_1+t_2}{U_2}\gamma_1 - \frac{t_3}{\varepsilon-U_1+2U_2}\alpha$	γ_2	$\frac{t_2-t_1}{U_2}\gamma_2 - \frac{t_3}{\varepsilon-U_1+2U_2}\beta_2$
Ψ_1^s		α	0	$\beta_1(\approx 0)$	$\frac{t_2-t_1}{U_2}\beta_1 - \frac{t_1+t_2}{U_2}\beta_2$
Ψ_2^s			α	$\frac{t_1+t_2}{U_2}\beta_1 - \frac{t_2-t_1}{U_2}\beta_2$	β_2
Ψ_1^a				α	0
Ψ_2^a					α

References

- 1 Atkins, P.; Overton, T.; Rourke, J.; Weller, J.; Armstrong, F. Shriver and Atkins' Inorganic Chemistry, 5th ed.; Oxford University Press, USA, 2010.